Acta Biomaterialia 162 (2023) 149–163

Contents lists available at ScienceDirect

Acta Biomaterialia

journal homepage: www.elsevier.com/locate/actbio

Full length article

# Earthworm granules: A model of non-classical biogenic calcium carbonate phase transformations

Sara Mandera[a], Ismael Coronado[b,*], Lurdes Fernández-Díaz[c], Maciej Mazur[d], Juncal A. Cruz[b], Bartłomiej Januszewicz[e], Esperanza Fernández-Martínez[b], Pedro Cózar[f], Jarosław Stolarski[a]

[a] Institute of Paleobiology, Polish Academy of Sciences, Twarda 51/55, PL-00-818 Warsaw, Poland
[b] Faculty of Biological and Environmental Sciences, University of Leon, Campus Vegazana s/n, ES-24071 León, Spain
[c] Department of Mineralogy and Petrology, Complutense University of Madrid, ES-28040, Madrid, Spain
[d] Department of Chemistry, University of Warsaw, Pasteura 1, PL-02-093 Warsaw, Poland
[e] Institute of Materials Science and Engineering, Lodz University of Technology, 1/15 Stefanowskiego, Lodz PL-90-924, Poland
[f] Geosciences Institute (CSIC, UCM), c/ Severo Ochoa 7, 28040-Madrid, Spain

ARTICLE INFO

*Article history:*
Received 24 August 2022
Revised 17 March 2023
Accepted 22 March 2023
Available online 29 March 2023

*Keywords:*
ACC
Biomineralization
CPA
Phase transformation
Short-range ordering

ABSTRACT

Different non-classical crystallization mechanisms have been invoked to explain structural and compositional properties of biocrystals. The identification of precursor amorphous nanoparticle aggregation as an onset process in the formation of numerous biominerals (crystallization via particle attachment) constituted a most important breakthrough for understanding biologically mediated mineralization. A comprehensive understanding about how the attached amorphous particles transform into more stable, crystalline grains has yet to be elucidated. Here, we document structural, biogeochemical, and crystallographic aspects of the formation as well as the further phase transformations of the amorphous calcium carbonate particles formed by cultured specimens of earthworm *Lumbricus terrestris*. *In-situ* observations evidence the formation of proto-vaterite after dehydration of earthworm-produced ACC, which is subsequently followed by proto-vaterite transformation into calcite through nanoparticle attachment within the organic framework. In culture medium spiked with trace amounts of $Mn^{2+}$, the cauliflower-like proto-vaterite structures become longer-lived than in the absence of $Mn^{2+}$. We propose that the formation of calcite crystals takes place through a non-classical recrystallization path that involves migration of proto-vaterite nanoparticles to the crystallization site, and then, their transformation into calcite via a dissolution-recrystallization reaction. The latter is complemented by ion-by-ion crystal growth and associated with impurity release. These observations are integrated into a new model of the biocrystallization of earthworm-produced carbonate granules which highlights the sensibility of this process to environmental chemical changes, its potential impact on the bioavailability of contaminants as well as the threat that chemical pollution poses to the normal development of its early stages.

**Statement of significance**

Understanding the mechanisms of nucleation, stabilization and aggregation of amorphous calcium carbonate (ACC) and factors controlling its further transformation into crystalline phases is fundamental for elucidation of biogenic mineralization. Some species of earthworms are natural workbench to understand the biogenic ACC, stabilization and the transformation mechanisms, because they create millimeter-sized calcareous granules from amorphous calcium carbonate, which crystallize to a more stable mineral phase (mostly calcite). This study undergoes into the mechanisms of ACC stabilization by the incorporation of trace elements, as manganese, and the ulterior precipitation of calcareous granules by a coupled process

* Corresponding author.
*E-mail address:* icorv@unileon.es (I. Coronado).

https://doi.org/10.1016/j.actbio.2023.03.034

of amorphous particle attachment and ion-by-ion growth. The study points to sensibility of this process to environmental chemical changes.



## 1. Introduction

Calcium carbonate is one of the most ubiquitous component used by invertebrates during the biologically mediated crystallization (biocrystallization) of hard tissues such as skeletons (e.g., corals, echinoderms [1,2]), skeletal parts (e.g., porifera, ascidians [3–5]), and storage deposits (e.g., crustaceans and earthworms [6,7]). Among carbonates, calcite and aragonite are the most common and relatively stable mineral phases occurring in nature, although some other phases such as vaterite (e.g., otoliths [8]) and monohydrocalcite (e.g tapeworms [9]) are also used by calcifiers. Biogenic mineral structures are composite materials formed by the assembly of organic (multi-)component (e.g., proteins, lipids and carbohydrates), water and mineral phase(s) in different proportions [10]. It is widely established that the crystalline structure identified in skeletons of many groups of calcifiers results from the crystallization of originally poorly ordered carbonate precursors (i.e., short- and medium-range order [11,12]). Such precursors like amorphous calcium carbonate (ACC) are transported to confined calcification sites [13,14], where they aggregate and form crystals by particle attachment crystallization (CPA [15]). This process is mediated by an organic insoluble hydrogel interface, which creates a mineralization scaffold [16]. Usually, amorphous calcium carbonate promptly transforms into crystalline phases, but it can also be stabilized by organic macromolecules, phosphate, silica, and $Mg^{2+}$ ions [17–20]. The involvement of organic polymers in biocrystallization processes (e.g., in corals, echinoderms or mollusks) results in formation of 'mesocrystals', which consist of co-oriented nanoparticles [14,21].

Several mechanisms have been suggested for the amorphous to crystalline stage transformation, including solid-state mechanisms, which may involve secondary nucleation phenomena [22,23] and dissolution co-precipitation processes [15,24]. Nevertheless, the most important challenge of biocrystallography is elucidating the factors that determine the emergence and stabilization of distinct calcium carbonate crystalline phases in various groups of organisms. To date, multiple biogenic and synthetic ACC forms with different level of hydration have been identified [25–27]. Furthermore, a variety of short-range ordered structures related to the anhydrous phases such as calcite (proto-calcite [28]) and aragonite (proto-aragonite [2,29]) have also been identified, giving rise to the concept of polyamorphism [12]. Other unusual short-range ordered precursors whose structures relate to that of hydrocalcite (proto-monohydrocalcite [30]) have been recognized in biogenic carbonates, whereas vaterite-like structural arrangements (proto-vaterite [28]) have been found in synthetic ACC. Some of these disordered phases seem to transform directly into final anhydrous phases: e.g., proto-calcite transforms into calcite in echinoderm spicules [31], proto-aragonite transforms into aragonite in freshwater gastropods [32,33] and corals [2,34]. Mass et al. [34] suggest that proto-aragonite (or aragonitic ACC) co-occurs with ACC and ACC-$H_2O$ and the concomitant occurrence of solid-state transformations and dissolution/co-precipitation processes. In contrast, synthetic experiments have highlighted that proto-structured ACC does not always transform into its dehydrated counterpart phase [28], most likely due to the important role that pH and the presence of additives in the crystallization media can play in determining both, the transformation mechanisms and the phase selection [12,35]. Some of the aforementioned mechanisms may implicate a redispersion (i.e., migration) and reassembly of the nanoparticles [36,37]. The later process should leave some structural and/or compositional evidence in the resulting mineral e.g., neoformation of porosity due to changes in molar volume between amorphous and stable phases [24] or redistribution of impurities such as trace elements that stabilize the ACC or assist its transport.

Herein, we used the amorphous calcium carbonate particles formed by one species of earthworms (Annelida, Oligochaeta) as a workbench to study the phenomena associated with the ACC into more stable $CaCO_3$ phases transformation. The earthworms secrete ACC particles in a colloidal fluid of calciferous glands [38]. These particles are then transported toward a pair of oesophageal pouches, where they coalesce and crystallize [39–41]. The final product is a solid calcareous granule that is later excreted by the organism to the soil during the casting process [42]. Spherical or sub-elliptical $CaCO_3$ granules of 0.5 to 2 mm in diameter mostly consist of calcite, although vaterite, aragonite and ACC have also been identified among their components [7,41,43]. The purpose of such mineralized structures formation still remains unclear. The following roles have been proposed for these structures: pH buffering of the internal body, adjustment of respiratory $CO_2$, and elimination of excess of Ca derived from diet and even spurious mineralization [39,44–46]. The first characterization of amorphous calcium carbonate in earthworms was conducted by Kelly [47]. Its formation into the calciferous glands was studied by Gago-Duport et al. [41] and in granules by Lee et al. [7]. Rodríguez-Blanco et al. [48] suggested that the transformation of ACC to calcite in earthworms occurs via vaterite while Hodson et al. [43] argued that differences in amino acid concentration could explain the stabilization of disseminated ACC deposits within granules. The earthworm granules also seem to be sensitive to soil trace elements, whose presence seems to control the resulting carbonate mineralogy (e.g., cerussite [49]; vaterite [50]; aragonite [51]). Furthermore, earthworms remove metal and organic contaminants from soils and incorporate them into granules playing an effective soil bioremediation role.

The purpose of this paper is to elucidate the mechanisms involved in the transformation and/or recrystallization of poorly ordered precursors into stable mineral phases during the biocrystallization of earthworm granules, by applying a multi-analytical approach.

## 2. Material and methods

### 2.1. Material

Calcareous granules produced by earthworms were obtained from laboratory culturing of fully clitellate specimens of *Lumbricus terrestris*, which were sourced from Verme Deluxe (Zamora, Spain). Specimens were kept in artificial previously sieved to $< 500$ µm soil, which comprised 20 wt% peat moss, 18 wt% kaolinite and 62 wt% quartz sand. Artificial soil (250 g) and specimens were held in polypropylene vessels at constant temperature of 15°C in a refrigerated chamber, above-neutral pH ($CaCl_2$) by adding 2.5% of $CaCO_3$, and under controlled moisture (25 %w/w, hence 80% of the water holding capacity). Earthworms were fed with shredded sulfur-free

paper every week. All the reagents used were analytical grade and milli-Q water (resistivity 18.2 MΩ·cm at 25°C; filtered through a 0.22 μm membrane) was used in the formulation of the artificial soil and solutions.

The growth dynamics and recrystallization processes of granules were studied, for first time, in Mn-labelling experiments. Different Mn-sources were selected with the indirect purpose of understanding whether the sorption of Mn by earthworm granules could be produced through two mechanisms, the dissolution of previous $CaCO_3$ and/or the direct sorption from solution (i.e., soil water). Therefore, two Mn-sources in separate lines of trials were used during the labelling experiment: 1) Mn-bearing $CaCO_3$ (at 50 and 100 ppm, respectively), replacing the pure $CaCO_3$ from artificial soil; and 2) a $MnSO_4$ aqueous solution (100 ppm of Mn), replacing the pure water from the artificial soil. Mn-bearing $CaCO_3$ (100 and 50 ppm concentration) was precipitated by mixing 0.5 M $Na_2CO_3{\cdot}H_2O$ (Sigma-Aldrich), 0.5 M $CaCl_2$ (Sigma-Aldrich) solutions and 0.8 mM and 0.4 mM of $MnCl_2{\cdot}4H_2O$ (POCH) under continuous magnetic stirring during 30 minutes. Afterwards, the solution was filtered using a cellulose 0.45 μm filter and the recovered precipitate was dried overnight at 60°C. The original 100 ppm Mn solution was prepared by dissolving $MnSO_4{\cdot}H_2O$ (Labkem) in milli-Q water, energetically stirring, and subsequently filtering.

Seventeen specimens were cultured in laboratory, five control specimens during 28 days in an Mn-free soil with precipitated pure $CaCO_3$ (POCH) and milli-Q water, and twelve specimens in amended Mn-soil (4 for each composition, 100 and 50 ppm of Mn-bearing $CaCO_3$, and 100 ppm of $MnSO_4$ solution, respectively). Specimens were exposed to amended soils and Mn-free soils every 2 until reaching 14 days of experiment and 7 days until reaching 28 days. Calcareous granules were studied *in situ* (by oesophageal dissection and micro-computed tomography of specimens from control experiment) and *ex situ* (by retrieving and picking granules from the casting activity from control and Mn-experiment).

#### 2.1.1. In situ material

Two control specimens were narcotized in 30% alcohol, one was preserved in pure isopropanol before micro-computed tomography (micro-CT) scanning, which was placed and fixated in a polypropylene Falcon tube. Another specimen was dissected in pure isopropanol in order to retrieve the solid mineral concretions stored in oesophageal pouches. Pure isopropanol was used in both procedures with to avoid the spurious ACC transformation of the mineral concretion due to the inevitable partial dehydration of biological tissues. The mineral concretions retrieved were rinsed and cleaned in pure isopropanol and dried overnight.

#### 2.1.2. Ex situ material

After 28 days, earthworms were removed from the soil, rinsed with milli-Q water, and held in free-Mn vessels. Artificial soil was dried at 60°C, sieved to <500 μm to recover excreted granules by hand-picking them with tweezers under a binocular microscope. In addition, to facilitate removal of soil particles attached to granules and avoid ACC transformation, granules were cleaned by consecutive immersion in a 1 M NaOH solution and pure isopropanol and 2 minutes ultrasonication, and subsequently filtered. In order to test how the water held by the soil could affect the stability of different calcium carbonate phases produced by the Mn-labeling, after living in an Mn-amended soil during 28 days, a specimen from each experiment was placed into a Petri dish on a wet filter paper. Under exhaustive surveillance of specimens, fresh expulsed granules were retrieved after elapsed times not longer than 3 days. These granules were then cleaned and rinsed following the procedure described above.

After retrieving, some granules were studied and characterized in raw, other by natural breakage and some were embedded in epoxy resin, polished until the maximum diameter of the particle and consequently thin-sectioned (ca. 30 μm thick).

### 2.2. Methods

Structural and mineralogical characterization of *in situ* and *ex situ* materials was carried out, using micro-computed tomography (micro-CT), petrographic microscopy, cathodoluminescence (CL), scanning electron microscopy (SEM), field-emission scanning electron microscopy with energy dispersive spectroscopy (FE-SEM/EDS), confocal laser scanning microscopy (CLSM), electron microprobe analysis (EMPA), electron backscatter diffraction (EBSD), and Raman spectroscopy.

Whole natural samples from dissection and those retrieved from control and experimental soils were used for SEM and Raman spectroscopy previous mounting in aluminum stubs and fixed by carbon tape. Moreover, sample fragments obtained by means of natural breakage of the granules were also prepared for SEM and Raman analysis. Uncovered ultra-polished thin sections from control and amended soil granules were prepared for petrographic observation, EMPA, CLSM, CL, Raman spectroscopy and EBSD. Selected samples were etched with 0.1% formic acid and 2.5% glutaraldehyde for 1 minute, rinsed with ultrapure water (Milli-Q) and dried in air.

#### 2.2.1. In situ methods

Micro-CT examinations were collected by using a MicroXCT-400 system (XRadia, Zeiss microscopy GmbH, Germany) located at the Faculty of Materials Science and Engineering, Warsaw University of Technology. Scanning of *ex situ* calcareous granule and *in situ* earthworm body were performed using the following parameters: 60 kV (granule) and 40 kV (body) of voltage, 10 W, 5 s of exposure time, 2.4 μm (granule) and 5.4 μm (body) of pixel size and 1000 projections per sample. Radial projections were reconstructed with XMReconstructor software provided with the Zeiss XRadia system. Three-dimensional rendering of earthworm tissue with calcareous granules was obtained by processing with the AVIZO7.0 Fire Edition software.

#### 2.2.2. Ex situ methods

Petrographic microscopy observations were conducted on 51 thin sections of both, control and experimental granules, in transmitted and polarized light with a Nikon Eclipse 80i microscope equipped with a DS-5M cooled camera head (Institute of Paleobiology of the Polish Academy of Sciences, Warsaw).

Scanning Electron Microscopy (SEM) observations were performed after platinum coating using a Philips XL–20 (Institute of Paleobiology of the Polish Academy of Sciences, Warsaw) with accelerating voltage of 25 kV, ~8 mm of working distance and ~5 μm of beam diameter and with Field – Emission Scanning Electron Microscopy (FESEM, Zeiss Merlin) equipped with an EDS detector (Department of Chemistry, University of Warsaw) with accelerating voltage of 5 kV, ~4 and ~6 mm of working distance for imaging and 15 kV and ~6 mm for EDS measurements.

Cathodoluminescence (CL) microscopy was performed on carbon coated thin sections using a HC5-LM microscope equipped with a Lumic hot cathode and linked to a CCD Kappa camera for recording images (Institute of Paleobiology of the Polish Academy of Sciences, Warsaw). An electron energy of 14 keV, beam current of 0.18 mA and variable exposure time were used.

Confocal Laser Scanning Microscopy (CLSM) observations were conducted on Mn-labelled samples in thin sections using a Nikon Eclipse Ti equipped with VIS-lasers linked to a CCD DS-5Mc video camera with resolution 5 Mpx (Department of Biology, University of Warsaw). The wavelengths used are as follows: 404 nm, 488 nm,

561 nm and 638 nm, 32-channel spectral detector with resolution 2, 5, 6 or 10 nm and mode Virtual Filter, and transmitted light.

Electron Microprobe Analysis (EMPA) mapping and punctual analysis were carried out on thin sections with a 25 nm carbon coating, with a JEOL Superprobe JZA-8900 with five wavelength-dispersive spectrometers, at the National Center of Electron Microscopy (Complutense University of Madrid, Spain). The measurements were conducted in nine elements (Ca, Mg, Sr, Na, Ba, S, Fe and Mn) on the whole granule. An accelerating voltage of 20 kV with a beam current of 50 nA and a spot size and step interval of 1 µm diameter (dwell time = 20 ms) were used. Some punctual analyses of the same elements were performed using an accelerating voltage of 15 kV, a beam current of 10 nA and a spot size of 5 µm to accurately measure the chemical composition of granules during the experiments.

Electron backscatter diffraction (EBSD) was performed on thin-sectioned samples mechanically polished in advance with alumina of 9 µm, 1 µm, 0.3 µm and finally with colloidal silica (0.05 µm). Before analysis, samples were cleaned, dried and coated with the thinnest possible conducting carbon layer (c.a. 2–4 nm) using a BALTEC SCD 005 sputter coater. The EBSD study was carried out with an Oxford NordlysMax detector mounted on a Scanning Electron Microscope (SEM) JEOL JSM-6610LV at the Institute of Materials Engineering, Łodz University of Technology. EBSD data were collected with AztecHKL software at high vacuum, 20 kV, large probe current and 20 mm of working distance. EBSD patterns were collected at a resolution of 0.22 µm step size and data were processed using MATLAB$^{TM}$ toolbox MTEX [52].

Thermal gravimetric analysis (TGA), differential thermal analysis (DTA) and differential scanning calorimetry (DSC) were carried out using a TA Instruments thermobalance model SDT-Q600 with 0.1 µg of balance sensitivity, located at CAI of Geological Techniques of Complutense University of Madrid (Spain). Powdered granules (15 to 20 mg), held in platinum pans, were heated under a linear gradient from ambient (c.a. 20°C) up to 1000°C; heating rate: 10°C/min under a $N_2$ atmosphere, with flux fixed to 100 ml/min. Granules from different experiments were analyzed measuring the weight loss, derivative weight loss and differential heat flow. Before the analysis, the baseline, DSC precision and temperature were calibrated internally by the laboratory up to five times with different protocols.

Raman spectra were collected with a LabRAM HR Raman confocal microscope equipped with an LPF Iridia edge filter and a Peltier-cooled Synapse CCD detector, located at Department of Chemistry, University of Warsaw (Poland). The microscope attachment was based on an Olympus BX41 system with an MPLN1003 objective. The excitation source was the second harmonic of the diode-pumped Nd: YAG laser Excelsior-532-100 operating at 532.3 nm with 20 mW power on the sample. Benzerara et al. [35] observed that such laser power could cause some crystallization artifacts on amorphous materials. Such changes were not observed during our analyses, probably because the epoxy resin prevents or slows the crystallization of amorphous phases.

## 3. Results

### 3.1. In situ *observations: biocrystallization*

The first section of the Results provides a description of *in-situ* observations based on micro-CT examinations of VIII to XV segments of *Lumbricus terrestris* (Fig. 1) and the morpho-structural and mineral characterization of the calcareous products after dissection (Fig. 2). These observations contribute to the understanding of the biocrystallization process of granules.

X-ray images reveal three tissues based on density (gray scale coloration, Fig. 1C): 1) Soft body tissues of earthworm (i.e., body wall, coelomic cavity, and digestive system) characterized by low-dense material (dark gray). Several 2D sections disclose the gut lumen in the center, and more specifically oesophageal portions partially filled with air (Fig. 1C). Rendered surface shows ana-

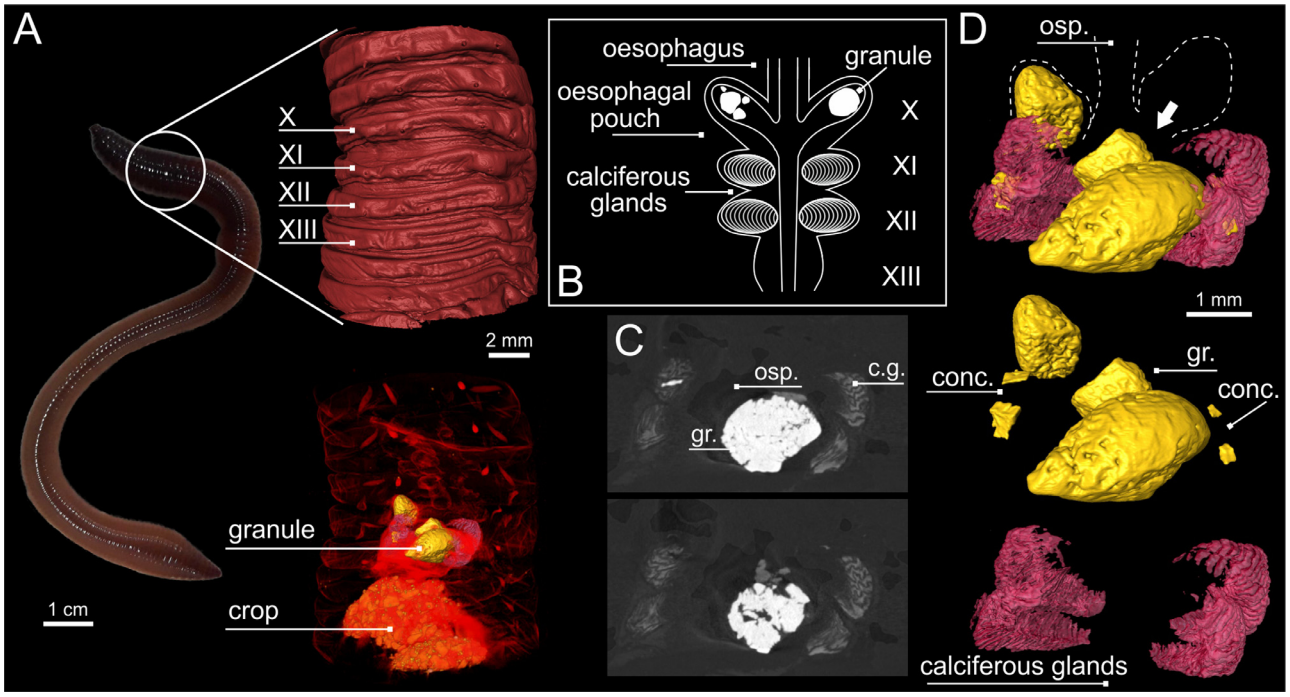


**Fig. 1.** Formation of earthworm granules. (A) Example of living earthworm (*Lumbricus terrestris)* and micro-CT images from anatomical external (upper) and internal (bottom) details of the segments VIII-XV. (B) Scheme of oesophagal parts where the ACC and the concretions are produced (based on Canti and Piearce, [42]). (C) X-ray images of granule in the oesophagal lumen and the calciferous glands with their characteristic "zebra" pattern. Note the porosity of granule visible in different planes images and on the upper picture noticeable structure of the same density as the granule in the pouches. (D) micro-CT rendering of the calciferous glands with small concretions inside, two granules in the oesophagal lumen and a granule under formation into the pouches. cg: calciferous glands; conc: concretion; gr: granules; osp: oesophagus.

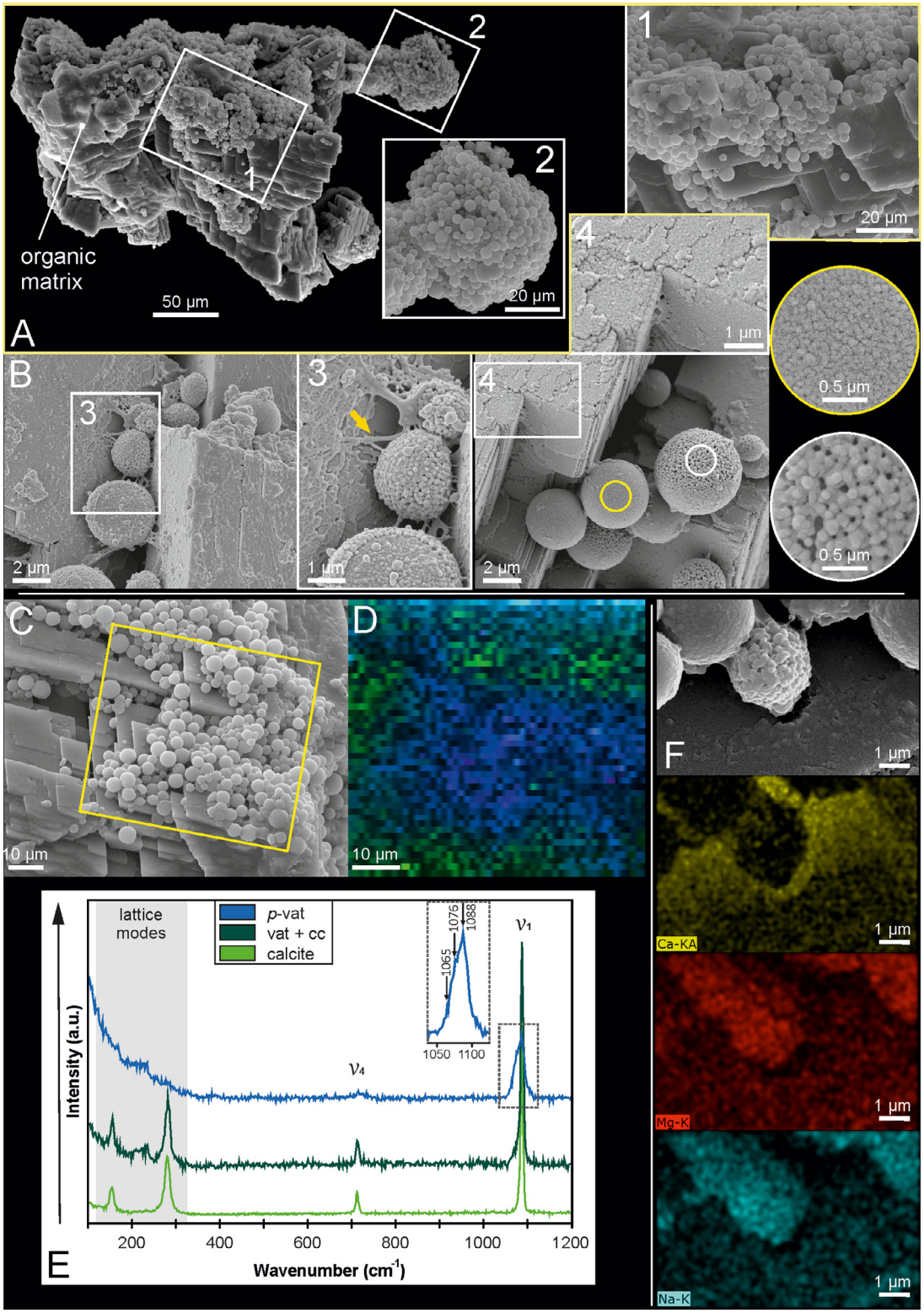


**Fig. 2.** Carbonate particles isolated from the pouches during dissection. (A) SEM image of a dissected concretion composed of subhedral-anhedral carbonate particles (A.1) and spherulites (A.1, A.2). (B) Calcite crystals and proto-vaterite spherulites and the organic matrix covering both (yellow arrow, B.3) at high magnification. Proto-vaterite spherulites are composed of nanoparticles and their surfaces can be smooth (blue inset) or rough (green inset), and calcite crystals exhibit mesoporous and stepped faces (B.4). (C-E) Raman analysis of the dissected concretion. Raman map (C) of the selected area (yellow square) at SEM picture (D, note that the sample is rotated) and Raman spectra (E) of proto-vaterite, vaterite and calcite. Spectra colours correspond with the appropriate phase in the Raman map. (F) EDS maps of area showed at (B) image. EDS maps showing distribution of calcium (Ca), magnesium (Mg) and sodium (Na). Proto-vaterite spherulites are Mg- and Na-enriched (more intensive colour) in Ca-depleted than calcite crystals surrounding. *p*-vat: proto-vaterite; vat: vaterite.

lyzed segments partly dehydrated and setae pairs (Fig. 1A). 2) Partially mineralized tissues, characterized by medium dense materials (mild gray, Fig. 1C), are located surrounding the central gut in two pairs of subspherical sacs in the segments XI and XII. These areas are characterized by oesophageal enlargements (i.e., calciferous glands) with a zebra patterned slightly zigzagging organization (Fig. 1D). 3) High-dense mineralized materials, characterized by a white coloration, are located between the X to XIII segments. Three large mineralized spheroidal to ellipsoidal particles with coarse surface, about 1-2 mm in size, have been identified (Fig. 1D), two in the central part of the gut lumen, between XI-XIII segments, and another inside a lateral oesophageal pouch (subspherical sac), in the segment X. Four small mineralized-particles, submillimeter-size, were localized interbedded with partially mineralized material into the calciferous glands, forming irregular sheets or subhedral to anhedral particles. High-dense particles located from the XV segment in the posterior foregut (i.e., crop-gizzard area, Fig. 1A, bottom) have been identified as soil particles (*sensu* [53]) and excluded for further considerations.

Subhedral-anhedral, submillimeter-sized, carbonate particles were isolated from the pouches during dissection (Fig. 2). Morpho-structural study revealed these particles are composed of crystals with stepped and well-developed faces surrounded by spherulitic material and organic tissues (Fig. 2A and B). Micrometric-sized rhombohedral calcite crystal, tens of micron-sized and randomly organized, were identified by its distinctive well-developed (104) faces in subhedral areas and confirmed by micro-Raman analysis (*sensu* [25]), $\nu 1$ at 1088 $cm^{-1}$ and $\nu 4$ at 715 $cm^{-1}$ of the $(CO_3)^{2-}$ groups, lattice modes region at 284 $cm^{-1}$ and 158 $cm^{-1}$ (Fig. 2D-F).

On the other hand, anhedral areas are characterized by large aggregates of spherules and emerging visible calcite faces (Fig. 2B). Micrometric-sized spherules (1.5-5 μm) exhibit variable morphologies from perfect spheres to half-spheres with smooth and rough surfaces. High-magnification observations expose mesoporous coarse calcite faces composed of nanoparticles (tens of nanometers-sized) mostly in kinked and stepped faces and the interface between crystals. Moreover, spherules show coarse surfaces formed by nanoparticles with different particle size, in spherules with smoother surfaces nanoparticles are ca. 80 nm in size (Fig. 2B, yellow circle), but in those with rougher surfaces nanoparticles are ca. 115 nm in size (Fig. 2B, white circle). Rough spherules have distinctive mesoporous surfaces with pores of 120-240 nm in size (Fig. 2B). Spheres and calcite crystals are enveloped by an organic network (Fig. 2B, yellow arrow) and transitional products between spherules and calcite faces can be observed. Smooth spheres become porous and rougher and begin to collapse, producing half-spheres and/or irregular aggregates of nanoparticles coating calcite crystals. Raman analyses of spherules disclose a triplet in the symmetric stretching region of $(CO_3)^{2-}$ groups, $\nu 1$ at 1065, 1076 and 1088 $cm^{-1}$ characteristic of vaterite (sensu [25]), but $\nu 4$ and lattice modes are irregular and do not show intense enough peaks, which suggest a disordering of the crystal lattice (Fig. S1). Raman mapping shows spectra with features that are a mixture of those characteristic of disordered vaterite and calcite, generally in anhedral areas with irregular nanogranular masses coating the calcite crystals. This suggests a transitory coexistence between both phases in those areas. EDS elemental mapping shows that spherules are Mg- and Na-enriched and Ca-depleted, in contrast to those observed for calcite crystals (Fig. 2F).

### 3.2. Control samples: regular growth

The number of granules and weight of $CaCO_3$ produced by adult samples of *Lumbricus terrestris* was calculated by counting and weighing the recovered granules after experiments. The production of granules in control samples after 7 days is variable and depend on the specimen (from 3 to 5 granules). The amount of $CaCO_3$ produced per specimen is more constant than the number of granules production, ca. 1.05 mg/day (Table S1), this variation is due to the variable size of the granules.

Spherical to sub-elliptical (e.g., kidney-shaped, Fig. 3 A-C, G-I, L) $CaCO_3$ calcareous granules from 0.5 to 2.5 mm in diameter were recovered from control samples (24 granules in total). Granule edges are frequently smooth in spherical specimens, although sub-elliptical granules have an irregular side with a cockscomb habit (Fig. 3C, L). Petrographic observations under crossed polarization show that granules are mostly composed of radially arranged carbonate crystals of 0.015 to 0.2 mm in size (Fig. 3A-C), occasionally radiating from a chaotic center formed by smaller crystals, and sometimes arranged around void central areas and large isolated pores (Fig. 3B-C, K). A large variation of microstructures is present in granules: prismatic-blocky (Fig. 3A-C, L), lath-radial, and foliated–lamellar crystals, which occasionally are arranged forming cross-lamellar-like microstructures and interlocked blocks, depending on the granule (Fig. 3L). All of them at SEM exhibit the characteristic (104) and tautozonal planes of calcite crystals. It should be highlighted the existence of high inter-crystalline porosity, mostly within those granules with cross-lamellar-like and interlocked blocks microstructures (Fig. 3L, red arrow). This porosity is equivalent to that observed in the X-ray images of micro-CT scans (Fig. 1C). Opaque impurities in transmitted light, irregularly concentrically arranged but also located radially in the crystal contact and inside crystals are a distinctive feature of these structures. EBSD analyses reveal that control-granules exclusively consist of randomly arranged calcite crystals without significant internal misorientations within each crystal (Fig. 3D-F).

Under cathodoluminescence microscopy, cross-sectioned granules disclose a concentric pattern defined by alternating luminescence bands unevenly distributed (Figs. 3A-C). Those areas with cockscomb habit in the edge of granules as well as some granule cores exhibit kinked bands, whereas smooth granules exhibit undulatory or even stromatolite-like patterns. Moreover, some areas and small dots, mostly corresponding to opaque impurities, exhibit higher luminescence. The thickness and number of bands have been measured in seven granules using the plug-in ObjectJ 1.03w [54] of the free and open-source ImageJ 1.47v image processing software [55]. Band thickness and number of bands per granule is variable ca. 6-11 μm and ca. 50-100 bands per granule. Number of bands also is directly related to the granule diameter and considering the quantity of granules formed after 7 days and the number of bands, it can be estimated that bands form sub-daily, one band every 0.5 to 1 hours.

Rendered micro-CT sections of a kidney-shaped granule evidence its external coarse structure (Figs. 3G, 3I), highlighting equivalent features as observed by SEM (Figs. 3L-N). The micro-CT sections of the internal part of the granule show inter-crystalline large, interconnected pores, further confirming observations by petrographic microscopy, EBSD and SEM observations (Figs. 3A-C, E, K, L). Additionally, rendered kidney-shaped granules, which are usually larger than rounded ones (not more than 2 mm), result from two granules merging. This explains the existence of two visible independent radial cores on the petrographic and CL micrographs (Figs. S2C-D).

Acidic etching with an organic fixative shows that calcite crystals are formed by microbands of different solubility. Less soluble bands are characterized by dense aggregates of rounded nanoparticles with ca. 100 nm in size, whereas more soluble bands exhibit less dense nanoparticles aggregation with equivalent size but higher porosity (Figs. 3M, N). It should be highlighted the presence of small rhombohedral particles of hundreds of nanometers also embedded in the nanotexture. Moreover, etching emphasizes the

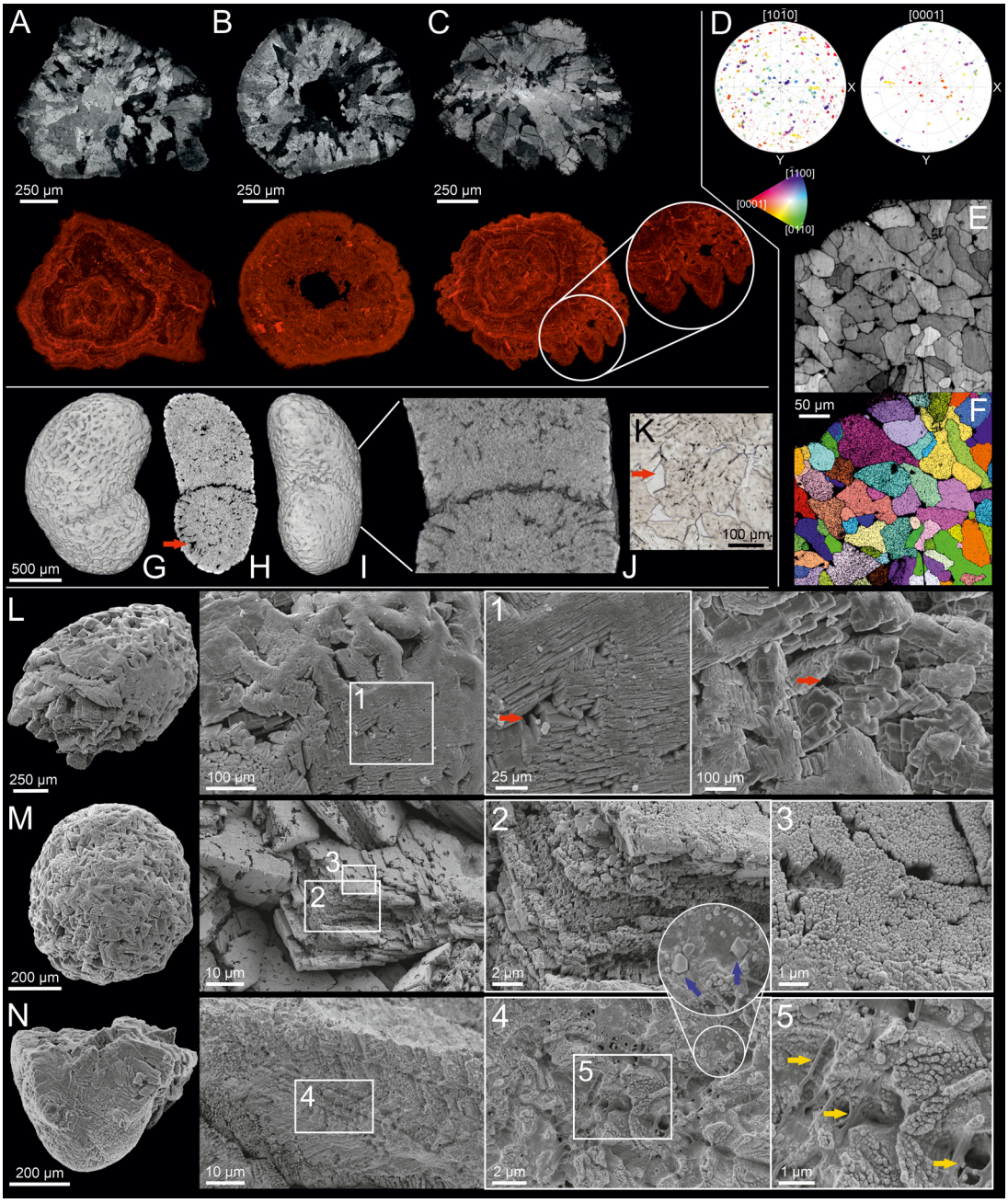


**Fig. 3.** Granules produced by earthworms in artificial not-amended soil. (A-C) Petrographic and CL images of thin sections showing the texture and the hidden cathodoluminescence pattern. Note that the morphology and microstructure of granule is variable. Granules are formed by radial calcite crystals with concentric luminescent micro-banding, occasionally kinked bands (C, inset). (D-F) Crystallographic arrangement of a granule. Pole figures (D), band contrast map (E) and crystallographic orientation map (F) showing random orientations of calcite crystals (EBSD). Colour-coding assigns a colour to each possible orientation. (G-H) micro-CT rendering of a kidney-shape granule showing that this kind of granule is composed by the attachment of two rounded concretions (J). (H, K, L) The internal macroporosity of the granules. Pores are indicated by red arrows in a micro-CT rendered section of the granule (H), in transmitted light (K) and in SEM (L). (L-N) SEM images showing the external morphology and structural features of excreted granules. Note the interlocked texture formed by lath crystals (L.1, M). Nanostructural features of granules after etching with 0.1% formic acid + 2.5% glutaraldehyde. (M.2, N). Differences in the solubility are highlighted by the micro-banding. Calcite fibres are formed by co-oriented nanoparticles surrounded by organic matrix (N.3, yellow arrow). It should be highlighted that some micro-rhombohedra (N.4, blue arrow) are observed.

presence of organic matrix that surrounds and coats both, calcite crystals and nanoparticles. The organic matrix consists in a network of interconnected nanometric fibers, which permeates and interlinks calcite crystals.

### 3.3. Experimental samples: Mn-amended soils

Granules grown in Mn-amended soils exhibit similar morphologies and sizes to those formed in control experiments. Earthworms were exposed to Mn-amended soils and free-Mn soils periodically (i.e., 2 and 7 days), with the purpose of characterizing the Mn-effect in the crystal growth dynamics and phase formation. $Mn^{2+}$ is a cathodoluminescence activator [56], which facilitates the identification of its recruitment by cathodoluminescence labeling when the final mineral phase is calcite and microstructural changes are not observable. Many granules show fibrous-radial aggregates, with a characteristic concentric convex fine banding (Figs. 4, S2). Occasionally these areas are in the core of the granule surrounded by

calcite crystals in straight contact and/or by isolated small pores (Figs. 4, S2C). Moreover, fibro-radial aggregates are dispersed into the granule as large or small patches surrounded by calcite crystals (Figs. S2 A-B). However, a significant minority of granules are totally formed by calcite crystals, without remnants of fibro-radial aggregates as confirmed by Raman and EBSD analyses (Figs. 4D-H).

Under cathodoluminescence (CL), fibro-radial aggregates exhibit higher luminescence than those calcite crystals grown in Mn-free soils and likewise, variations in luminescence are visible, forming bands or spot regions. Mn-labelling is confirmed in fully calcitic granules by luminescent areas (e.g., granule cores), surrounded by a non-luminescent or with dull luminescent bands area. Non-luminescent areas exhibit a luminescent intensity and banding like control experiments. Kidney-shaped granules formed by the accretion of two small granules exhibit differences in luminescence between the cores and the external parts in those Mn-labelled areas, regardless they consist of fibro-radial aggregates or calcite crystals (Figs. S2C-D).

Granules under confocal microscopy (CLSM) show that fibro-radiate aggregates exhibit intense auto-fluorescence regarding calcite crystals and stromatolite-like appearance in section. Confocal microscopy reveals that aggregates are formed by fine fluorescent banding oppose to luminescence detected under CL. Those areas with slight or non-fluorescence correspond to higher CL luminescent areas (Figs. 4A-B), and vice versa, although with subtle variations. Calcite crystals overgrowing the fibro-radial aggregates show weak fluorescence bands oppose to those dull-luminescent observed under CL (Figs. S2B).

Raman analyses of granules formed by fibro-radial aggregates disclose spectra with a triplet in the symmetric stretching region of $(CO_3)^{2-}$ groups, $\nu 1$ at 1065, 1075 and 1090 $cm^{-1}$, which are characteristic of vaterite. However, peaks in $\nu 4$ and lattice modes appear irregular and not intense enough to be attributed to any $CaCO_3$ phase (Fig. 4 E), similarly as observed in spectra collected during the *in-situ* characterization of dissected concretions (Fig. 2F). The absence of distinctive bands in lattice mode region in combination with the absence of Kikuchi patterns detected by the EBSD camera in the fibro-radial aggregates (Fig. 4H, S2) suggest a very poorly ordered lattice (i.e., amorphous nature). After a continuous electron beam is applied during tens of seconds in the same area some Kikuchi lines are detected by the EBSD camera, but they are not well defined enough for phase identification. The speciation of carbonate group in Raman spectroscopy and the development of Kikuchi lines along time suggest that fibro-radial aggregates are composed of the short-range ordered ACC, more specifically by proto-vaterite. On the other hand, by Raman and EBSD analyses confirmed that the adjoining area consists of randomly oriented calcite crystals (Fig. 4 E), despite its microstructure (i.e., radial microstructure Fig. 4A).

The Mn-source (i.e., $CO_3^{2-}$ or $SO_4^{2-}$) does not seem to induce visible changes in granule morphology and/or microstructure (Fig. 5). Cauliflower-like proto-vaterite aggregates are formed by sub-micrometric banding with characteristic differences in solubility after acid etching. Internally, banding is composed of fibro-radial nanocrystals of ca. 100 nm width (Fig. 5C). In those areas where the proto-vaterite to calcite transformation is noticeable, nanocrystals are densely packed defining distinctive calcite facets and mesopores into the crystals and adjacent areas (Fig. S5G-I).

Trace element composition is highly variable both between and within granules, and regarding Mn contents, it depends on the experimental setting. Those granules grown in 100 ppm Mn-amended soils are Mn-enriched (max. 1099 ppm) in comparison with those grown in 50 ppm amended soils (max. 473 ppm), evidencing that during granule crystallization earthworms uptake $Mn^{2+}$ in amounts conditioned by its availability. Granule areas consisting of fibro-radial proto-vaterite aggregates are enriched in Mg (max. 1065 ppm), Mn (max. 627 ppm) and S (max. 620 ppm) and Ca-depleted, in contrast to granule areas built up of calcite crystals (Fig. 6A), which are depleted in Mg (max. 60 ppm), Mn (max. 302 ppm) and S (max. 84 ppm) but enriched in Ba (max. 1083 ppm) at the same granule. In those granules formed almost completely by calcite and where the Mn-labelling is observed under CL, changes in Ca and Mg zoning are not observed, although systematically their cores are Mg- and Na- enriched and unexpectedly, non-luminescence bands or areas under CL are Na-enriched (Fig. 6, S4B).

Weight losses were calculated by TG-analysis in granules expulsed after 28 days-long experiment and granules buried in soil maximum times of 42 and 84 days, with the purpose of evaluating the variation in the content of different structural components as water (in all its forms) and organics (Fig. S6). The selected temperature range of study goes from room temperature ca. 20°C to 550°C, within which water and main organic components are decomposed in most of biominerals, well below the temperature at which the total $CaCO_3$ decomposition to CaO starts (~600°C) (Cuif et al., 2004). The weight loss curve of all granules mostly exhibits two main weight loss events, from room temperature to 250°C and from 250°C to 550°C. Granule weight losses within the thermal range analyzed vary between 1.12 to 1.63 wt% (Table S1). It is remarkable that those granules from experiments of 28 days have weight losses around 1.43-1.63 wt%, whereas those that remained longer buried in soil show smaller weight losses (1.33 wt% for 42 days and 1.11 wt% for 84 days).

## 4. Discussion and conclusions

### 4.1. Granule formation

Controlled biomineralization can be ascribed as the physiological and molecular processes by which organisms synthesize crystalline or amorphous minerals from aqueous solutions, assisted by metabolites and in confined spaces that contribute to regulate the supersaturation, the nucleation and growth processes and the final crystalline product [10,16]. Calciferous glands are the astonishing machinery that allows some specific earthworms to synthesize ACC particles in a similar way as crustacean produce gastroliths, although the function of such mineralization in earthworms remains unknown [43].

*In-situ* observations based on micro-CT scans revealed that the formation of ACC concretions and their ulterior transformation to crystalline structures mainly occur within the oesophageal pouches (Fig. 1-2) as was stated previously [7,42], although some submillimetric-size subhedral to anhedral particles are previously formed in the calciferous glands (Fig. 1D). It is assumed that these small concretions travel to the oesophageal pouches where conclusively coalesce. Labelling experiment confirm this interpretation, luminescent regions (by $Mn^{2+}$ labelling) can be concentrated in specific parts of granules, for instance in their core (Fig. 6, S2C-D), and they are produced by a labelling cycle. Nonetheless, they may also appear disseminated into the granule in a not labelled region, which suggests that some concretions enriched in $Mn^{2+}$ belatedly coalesce into the granule in cycles without Mn-labelling (Figs. 4A, 6C, S2A-B). Furthermore, this indicates that ACC spherulites can transform to calcite prior to granule formation, which is consistent with the Crang [57] and Gago-Duport et al. [41] hypotheses. Furthermore, results from the current study reveal that several granules can simultaneously be produced in one oesophageal pouch *sensu* Morgan [40], and even these may coalesce to form a single granule, as kidney-shaped granules with two luminescent cores are observed (Fig. S2C-D).

Calciferous glands of earthworms produce ACC regulated by organic macromolecules [40,41,43,57], whose presence retards $CaCO_3$

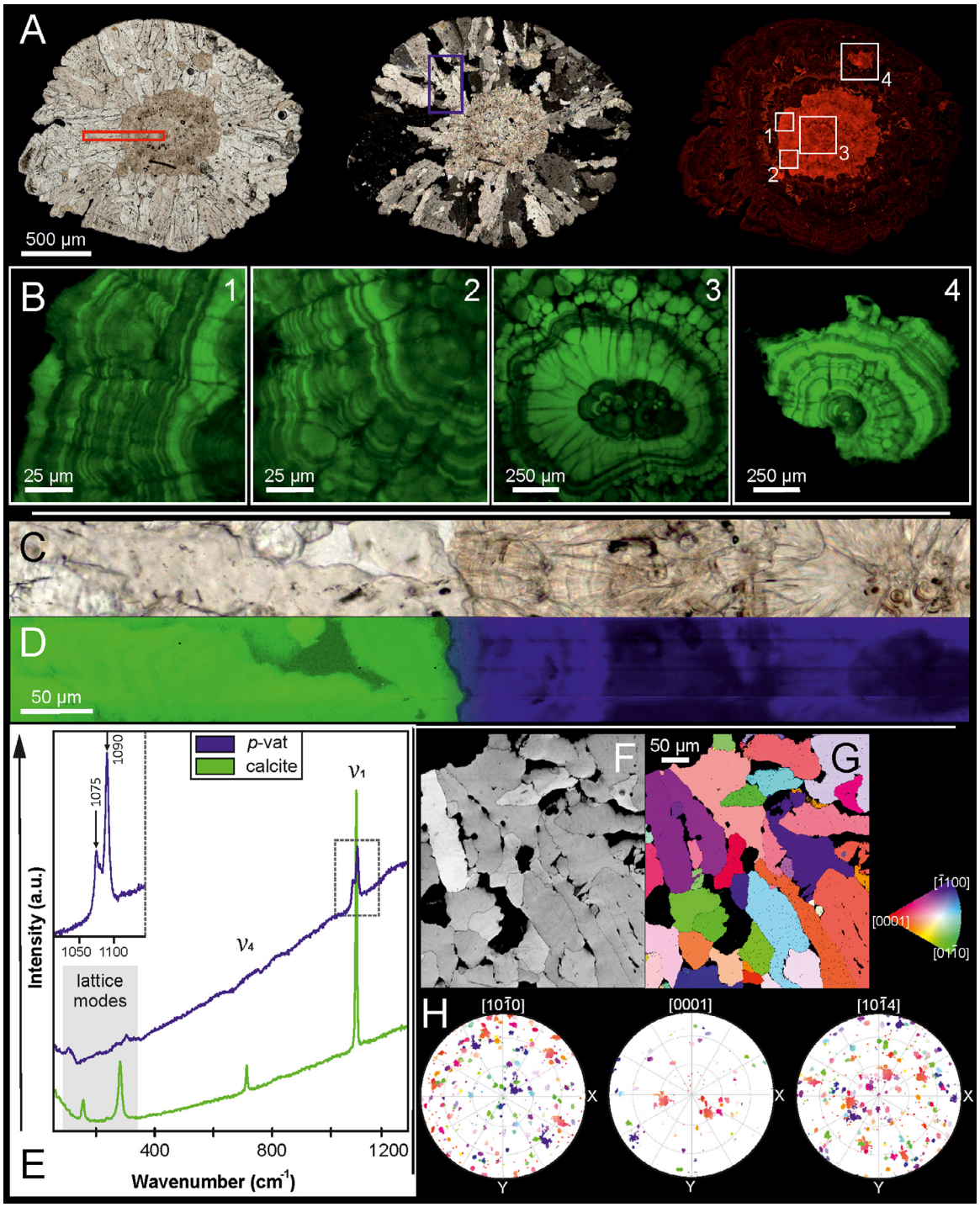


**Fig. 4.** Granules from Mn-labelling experiment. (A) Petrographic images in transmitted and polarized light, and CL images, showing the texture and the hidden luminescence pattern of labelled granules. Red square corresponds with Fig. 4C-D and blue square correspond with Fig. 4F-H. Luminescent central area caused by labelling is formed by proto-vaterite, whereas non-luminescent external area is formed by calcite. (B) CLSM images areas indicated in A (numbered squares in CL image) showing banding in proto-vaterite region (1-2) and revealing stromatolitic-like structure formed by micro-banding (3). It should be highlighted that a belated proto-vaterite concretion (4) is not in the labelled area. (C-E) Transmitted light image from a magnified area in A (red square in A), Raman mapping (D) of this area and Raman spectra (E). Map shows the contact between calcite (green colour) and vaterite (blue colour). Inset shows a detail of the characteristic triplet $\nu 1$ in the symmetric stretching region of $(CO_3)^{2-}$ groups of vaterite. Note that visible on the map darker parts in calcite area are pores. (F-H) Crystallographic features of the sample (EBSD). Band contrast map (F), crystallographic orientation map (G) and pole figures (H), showing rather random orientations of crystals but compared to regular growth granules (Fig. 3, D-F) (EBSD). Colour-coding assigns a colour to each possible orientation.

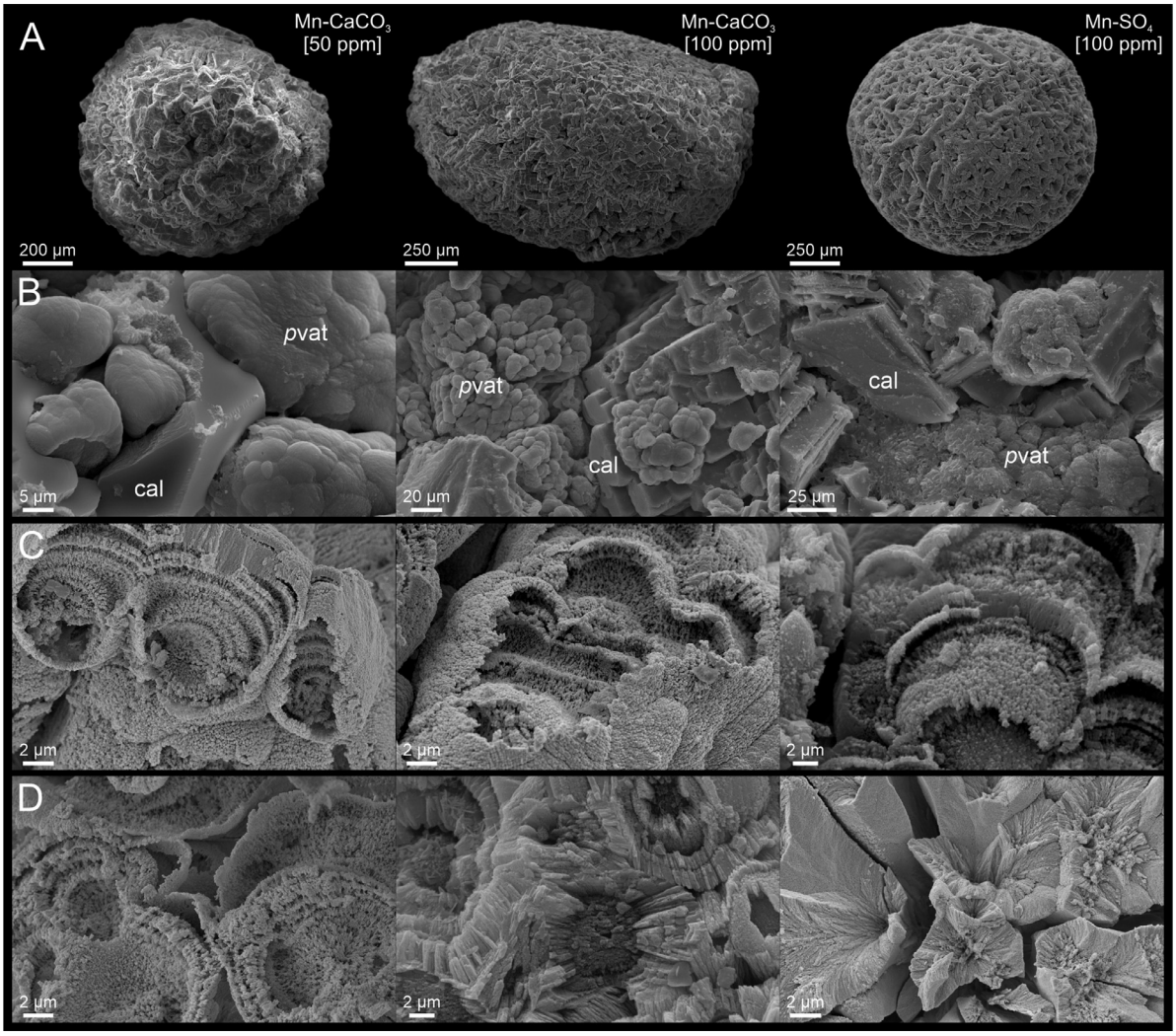


**Fig. 5.** SEM images of Mn-labelled granules formed by proto-vaterite and calcite. (A-C) Granules produced in three different Mn-amended soils. In all treatments coexisting calcite and vaterite can be found (B). (C-D) Cauliflower-like proto-vaterite particles are formed in all treatments, with a characteristic fibro-radial texture.

phase transformation, thereby efficiently facilitating mass transfer from the calciferous glands to the pouches and/or the development of accretion phenomena within the pouches. Although many species of earthworm (Crassiclitellata) may mineralize, not all of them (for example in *Eisenia foetida*) hold oesophageal pouches where $CaCO_3$ particles can coalesce to form granules [46]. Therefore, in those species that produce granules, these are $CaCO_3$ storage deposits whose final purpose is to be excreted.

Tailored microstructures and extremely well-organized crystallographic textures are main features of most skeletons and deposits produced by controlled calcifiers. In contrast, the results of our structural and EBSD analyses of *Lumbricus terretris* granules evidence a random crystallographic organization complemented by a large showcase of microstructures. In fact, the crystal growth is mainly featured by calcite crystals exhibiting complex penetration twins and competitive growth between crystals (Figs. 3L, S2I). These features suggest that during the final particle coalescence and crystallization processes that lead to the formation of granules in the oesophageal pouches the organism does not exert such expected control. Consequently, additional factors like the involved precursor phases and recrystallization processes as well as a variety of physicochemical characteristics of the crystallization medium (i.e., pH, supersaturation, trace element content) may influence the final product.

Granules exhibit characteristic concentric fine sub-daily bandings (0.5-1h/band) under CL which resemble those found in calcareous ooids (Figs. 3, S2). These bandings reflect oscillatory changes in composition regarding the amount of trace elements incorporated into $CaCO_3$ phases. These changes can affect $CaCO_3$ solubility (Figs. 3N, 5C-D). It has been demonstrated that concentric oscillatory compositional patterns arise during diffusion-controlled growth of solid solution crystals due to a complex interplay between the solubility of solid solution endmembers and the threshold supersaturation for end-members nucleation [58–61]. Differences in $CaCO_3$ solubility can explain the different etching behavior of adjacent concentric bands as depicted in Fig. 5C-D. Moreover, the compositional banding is coupled with different content of incorporated organics. Greiner et al. [62] observed concentric oscillatory patterns in the amount of polymeric matrix occluded by calcite crystals grown in agar gel. These authors interpreted that fast growth facilitates the incorporation of organics. Under a diffusive-regime, a period of fast growth results in the depletion of the growth medium and, as a result, is followed by a period characterized by a progressive drop in the growth rate and the amount of organics occluded. As mass transfer progresses, growth rate increases again, facilitating the incorporation of higher amounts of organics. Faster growth periods could also favor the incorporation of higher amounts of impurities like $Mn^{2+}$ or

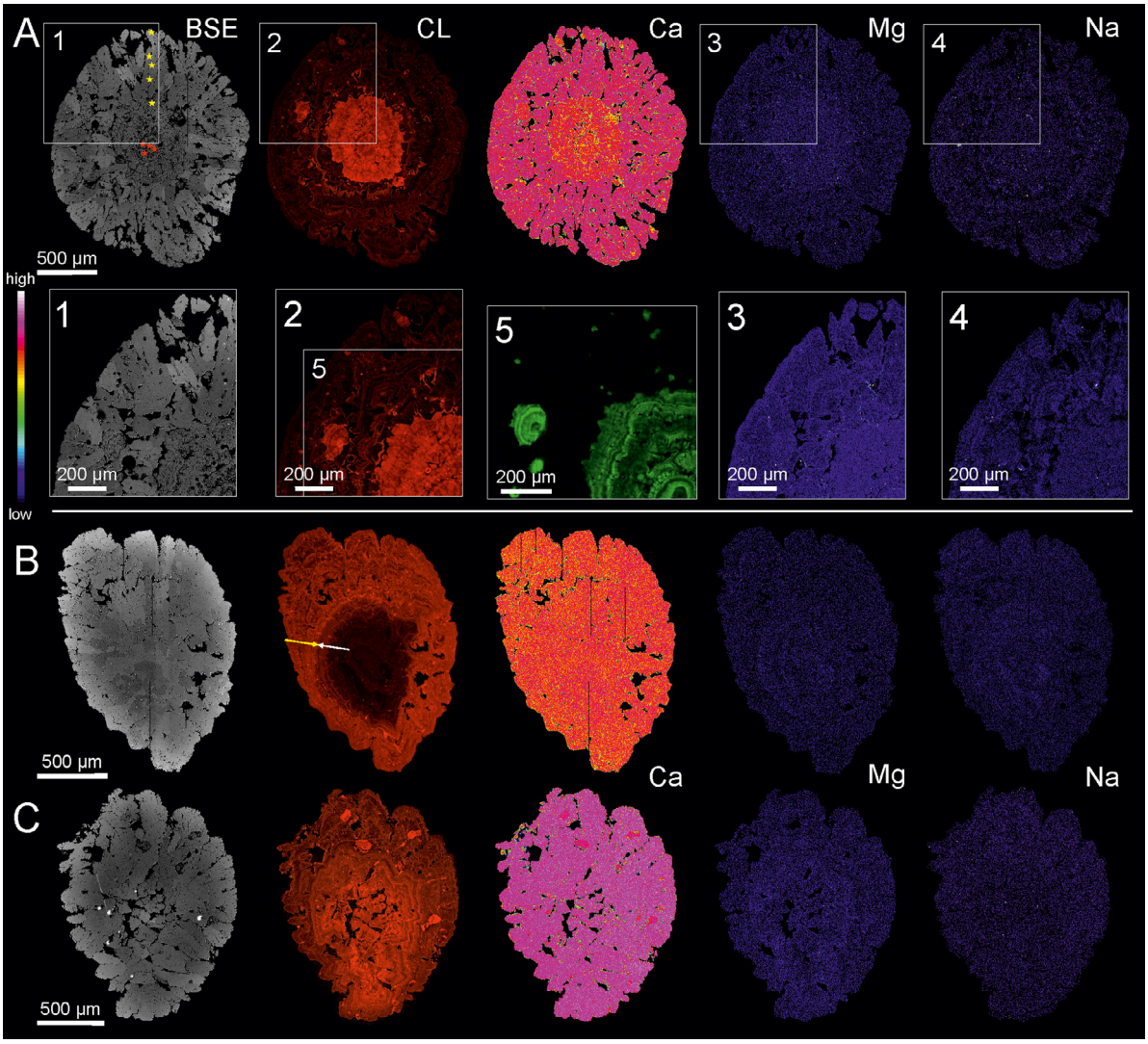


**Fig. 6.** Distribution of Ca, Mg and Na in Mn-labelled granules. Labelled area is in the centre of granule in (A) and (C), whereas in (B) labelled areas is the outer. BSE images, CL images, and EMPA maps showing strong correlation between carbonate phase and trace elements content. (A, C) Proto-vaterite areas are Mg- and Na-enriched and depleted of Ca. Higher amount of Mg corresponds with stronger luminescence laminate in proto-vaterite (compare A.3 and A.5, CLSM image). Punctual analyses (measurement areas marked with stars on A, BSE image, yellow stars in calcite area, green stars in proto-vaterite area).

$Mg^{2+}$, which would explain the association between higher concentrations of organics and trace elements in bands. Thus, concentric banding in granules would reflect sequences of growth cycles.

The presence of this banding suggests that granules grow by accretion around a central region. Bands often show irregular, occasionally undulatory, kinked or smooth profiles due to band merging and combining processes (Figs. 3A, 6, S2). Moreover, allochthonous particles have not been observed in the core of earthworm granules formed in our experiments. This is in contrast with observations in previous studies where allochthonous particles are described as accretion centers [7]. The central region of granules in this study shows a chaotic texture under CL. This texture is defined by several concentric micro-bands in prismatic crystals (Figs. S2). If we assume that the CL banding reflects the original biocrystallization pattern, with the final microstructure overimposed, changes in banding shape must denote differences in growth rates and crystallization pathways. Therefore, the central region of most granules has a chaotic appearance. This suggests the existence of an initial fast particle accretion event. This initial microstructure undergoes recrystallization processes that can involve phase transformations or dissolution phenomena that lead to the development of a central void (Figs. S2F, 3B). Additionally, some highly porous regions formed by calcite columnar crystals with cockscomb habit or by isolated large rhombohedral crystals show concentric oscillatory banding, clearly distinguishable within each crystal (Figs. 3C, S3). Accordingly, the sclerochronology of granules is very complex. This complexity is in part the result of subsequent recrystallization phenomena that take place after biocrystallization. On this premise, thin section petrographic observations, X-ray images from CT-scan and SEM imaging of granules reveal that the fibro-radial microstructure is less porous than the blocky and other related microstructures. Similarly, CL concentric oscillatory banding also appears more regular in the fibro-radial microstructure (Figs. S2E-F). These observations are consistent with the fact that the subhedral-anhedral crystals that built up dissected granules initially consist of polycrystalline mesoporous calcite crystals, while later, during or after granule excretion, granules undergo recrystallization (blocky to fibro-radial microstructure). Gago-Duport et al. [41] observed a similar morphological and microstructural evolution trend while studying spherulites of *L. friendi* by TEM: under the electron beam ACC particles transformed into calcite via vaterite and calcite microstructure evolved from a polycrystalline aggregate to a single crystal.

### 4.2. ACC transformation and non-classical recrystallization

Kelly (1901) characterized for the first time the amorphous nature of spherules formed in earthworm calciferous glands based on their features under polarized microscopy, followed by various investigations and techniques [39,41,43,57]. Amorphous calcium carbonate (ACC) particles in biogenic or *in vitro* precipitates are usually of nanometric size [6,26]. Intriguingly, the amorphous spherules found in earthworm calciferous glands (*Lumbricus terrestris* and *L. friendi*, [39–41]) are 1.5 to 5 μm in diameter, closer to the common size of vaterite spherules than that of most ACC particles [63,64]. However, some large ACC hemispheres have been precipitated in laboratory [24]. Gago-Duport et al. [41] described two kinds of spherules found after dissection of *L. friend*. These spherules showed significant differences in surface roughness, with those made up of ACC appearing smoother than those that consisted of vaterite nanodomains and calcite. Raman analyses conducted in this study confirm that smooth spherules from oesophageal pouches comprise short-range ordered $CaCO_3$ as there is an absence of well-defined bands in the lattice modes region of their spectrum. The presence of a triplet band in the $v1$ symmetric stretching region of $(CO_3)^{2-}$ groups suggests that this short-range ordered phase could be proto-vaterite. In contrast, the Raman spectrum of rougher spherules from oesophageal pouches exhibit better defined bands in the lattice mode region that can be assigned to vaterite (Fig. 2F). Raman spectroscopy has previously been useful for characterizing partially disordered biogenic and abiogenic carbonates: proto-aragonite in mollusks and corals, proto-calcite in synthetic carbonates [2,29]. It seems likely that ACC reorganization begins during particle transport from the calciferous glands to the oesophageal pouches, at which point some degree of short-range order has already developed in the spherules, as observed by Gago-Duport et al. [41]. This ordering is probably promoted by the partial dehydration of ACC particles. It must be noted that several authors have stated that the presence of small amounts of $H_2O$ in ACC plays a critical role in controlling its short-range ordering [24,65,66].

After labelling experiments, two biocrystallization pathways have been identified in earthworm granules (Fig. 7): one operates without $Mn^{2+}$ mediation and the other is $Mn^{2+}$-mediated.

#### 4.2.1. Regular formation of granules (Fig. 7: upper pathway)

$Mg^{2+}$ and $Na^{2+}$ enriched spherulites (Fig. 2C) precipitate in the calcification media (milky fluid) produced in the calciferous glands. These spherulites are bio-composites made of ACC and organic components, probably lipids, carbohydrates as well as some proteins or amino acids [41,43]. The presence of these organics stabilizes the spherulites, facilitating their transport [12,23] to the pooches and assisting their aggregation once there (Fig. 1). Spherulites undergo dehydration in the pouches, although it is likely that this process may start earlier as was abovementioned. Dehydration leads to an increasing roughening of the surface, which now appears formed by nanoparticles, as well as to the development of porosity (Figs. 2B, 7). This porosity is later enlarged as the water molecules released during the spherulites dehydration facilitates that some degree of spherulite surface dissolution takes place, further increasing the specific surface and the subsequent coarsening of proto-vaterite nanoparticles (Fig. 2B, 7). Bots et al. [67] proposed a similar sequence of processes to explain the *in vitro* ACC into vaterite recrystallization. In the system under consideration, the coarsening of proto-vaterite nanoparticles is followed by proto-vaterite reorganization to vaterite, as revealed by Raman maps. This structural reorganization causes a decrease in spherulite size and the release of calcium and carbonate ions to the crystallization bulk. Eventually, the collapse of proto-vaterite spherulites and the formation of calcite crystals takes place. Calcite formation may occur through two alternative mechanisms that may operate independently or simultaneously. One mechanism involves the progress of the dissolution of the precursor phase (proto-vaterite/vaterite) and the concomitant precipitation of the stable one (calcite). This reaction results in the release to the crystallization bulk of ions like $Mg^{2+}$, $Na^{2+}$ and $SO_4^{2+}$ groups, which were originally incorporated into the proto-vaterite (Fig. 7). The second mechanism involves the migration of nanoparticles to the growing faces of calcite crystals previously nucleated from the bulk (Fig. S5D) (*sensu* [36]). Calcite surfaces are mesoporous and stepped (Fig. 2B), and, according to the two mechanisms described, their growth may take place through the combination of nanoparticle attachment (i.e., CPA, *sensu* [15]), with the organic polymeric matrix acting as a scaffold, and a solution-mediated ion-by-ion classical growth mechanism. The later mechanism is supported by the presence of rhombohedral nanoparticles embed in the crystals (Fig. 3N.4-5). Similar $CaCO_3$ crystal formation processes have previously been observed by Gal et al. [37] in both, several organisms and the laboratory and more recently by Sun et al. [68] in the aragonite fibers of corals.

The development of mesoporosity in calcite surfaces may be the consequence of the negative changes in molar volume and solubility associated to the transformations between amorphous calcium carbonate (54.1 $cm^3\ mol^{-1}$; $Ksp_{ACC} = 10^{-6.0}$, [69]), vaterite (37.71 $cm^3\ mol^{-1}$, $Ksp_{vaterite} = 10^{-7.91}$ [70]) and calcite (36.9 $cm^3\ mol^{-1}$; $Ksp_{calcite} = 10^{-8.48}$, [70]) regardless of the mechanisms involved in them (Rodríguez-Navarro et al., 2015).

It should be noted that granules continue to evolve after they have been excreted by the earthworm. Once in the soil, granules gradually lose their organic matrix (Fig. S6) and the blocky calcite microstructure loses its mesoporous texture by cementation, generating a fibro-radial microstructure (Fig. S2E-F). The later suggests that the final recrystallization and cementation stages involve ion-by-ion growth and are probably controlled by the physico-chemical properties of the soil (such as pH, $CaCO_3$ saturation state, trace element contents, etc.).

#### 4.2.2. $Mn^{2+}$ mediated formation of granules (Fig. 7: lower pathway)

A second biocrystallization pathway has been inferred from observations of granule formation in the presence of $Mn^{2+}$. This pathway is characterized by a significantly longer stabilization of proto-vaterite, which does not totally dissolve in the experiment time framework. Our observations do not yield noteworthy differences between the first stages of ACC formation, transporting to pouches and dehydration in the biomineralization pathways operating in the $Mn^{2+}$-free and $Mn^{2+}$-bearing systems. Nonetheless, the presence of $Mn^{2+}$ stabilizes proto-vaterite spherules which reorganize into cauliflower-like aggregates. These aggregates are composed of a fibro-radial arrangement of nanocrystals of ca. 100 nm width, clearly apparent in cross-sectioned aggregates (Figs. 4-5). We assumed that mulberry-like aggregates found in *L. friendi* by Gago-Duport et al. [41], with an important amorphous component, and the stromatolite-like structures found by Lee et al. [7] in granule sections are equivalent counterparts to the cauliflower-like aggregates found in the granules produced in Mn-amended soils in this work. These authors concluded the amorphous nature of the mineral component from the absence of Kikuchi patterns in EBSD of their aggregates, suggesting that short-range order domains larger than few tens of nanometers are required to produce Kikuchi patterns. In this study, the amorphous nature of cauliflower-like aggregates concluded from EBSD results is further confirmed by the features of their Raman spectra, which lack any well-defined band in the lattice-vibration region. However, Raman spectra of cauliflower-like aggregates show some peaks characteristic of vaterite in the $CO_3^{2-}$ symmetric stretching region. Moreover, these structures exhibit optical birefringence under polarized

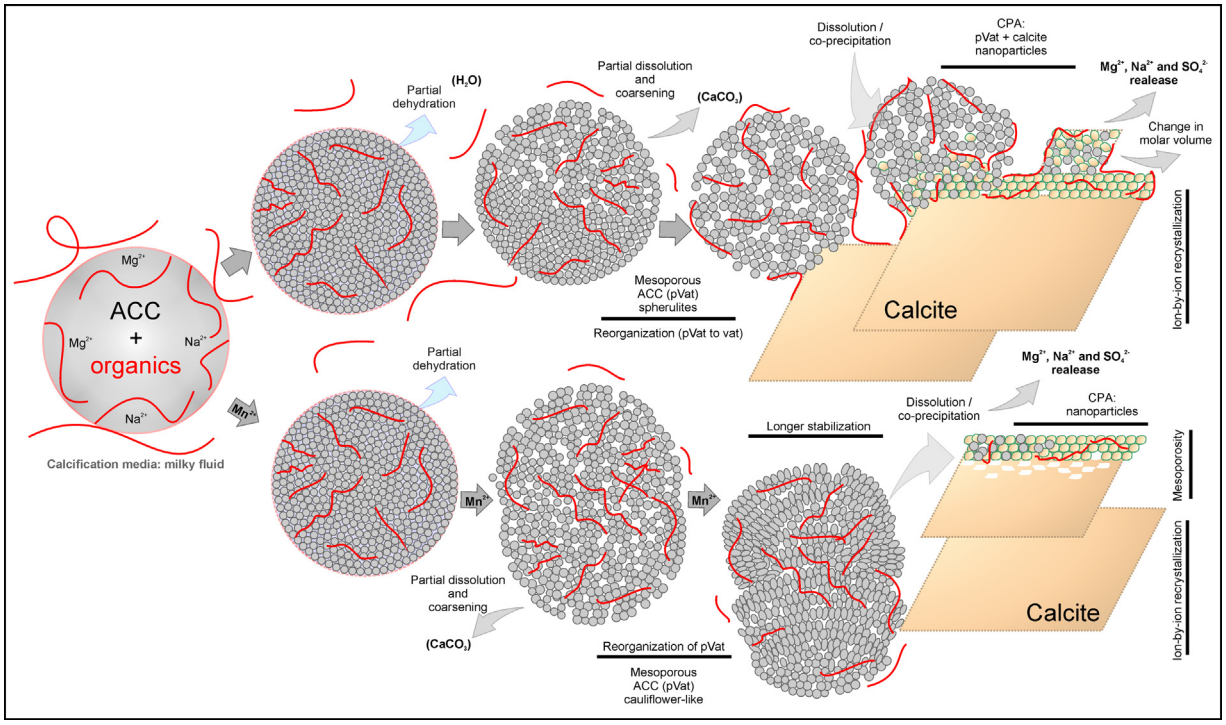


**Fig. 7.** Model of the proposed crystallization pathways in earthworm oesophageal pouches. The upper pathway represents regular crystallization without $Mn^{2+}$ mediation whereas the lower pathway represents the proto-vaterite stabilization caused by incorporation of $Mn^{2+}$ and its subsequent recrystallization to calcite.

microscopy. Both results are indicative of the existence of proto-vaterite short-range ordering (e.g., 400–700 nm).

Cauliflower-like aggregates consisting of radially arranged crystals are recurrent in vaterite, a $CaCO_3$ phase that can precipitate from supersaturated solutions in the absence as well as in the presence of additives like different alcohols, urea, amino acids [71–73]. In general, additives play an important role in promoting the crystallization of metastable phases and have been reported to stabilize vaterite [74]. *In vitro* vaterite precipitation experiments in the presence of $Mn^{2+}$ revealed that this ion becomes incorporated into vaterite via adsorption, contributing to decrease the solubility of this phase and slowing down the kinetics of the vaterite – calcite transformation [75]. Indeed, $Mn^{2+}$ is a recurrent cation in biogenic vaterites such as those in pearls and otoliths [8,76], usually coupled with higher concentrations of Mg, S and organics than found in other $CaCO_3$ phases [76]. Here, we find that proto-vaterite regions are enriched in Mg, Mn and S and depleted in Ca compared to calcite crystals. Furthermore, the high autofluorescence under CLSM in proto-vaterite regions suggests that this phase is also enriched in organic macromolecules. $Mg^{2+}$ and organic enrichment in proto-vaterite areas plays a two-fold role: (i) stabilization of ACC particles during transport (Fig. 2C) as the high hydration energy of $Mg^{2+}$ inhibits ACC dehydration [20,43]; and (ii) subsequent mid-term stabilization of proto-vaterite combined to $Mn^{2+}$ uptake (Fig. 6A). It is noteworthy that heterogeneously distributed ACC was previously identified in granules produced by earthworms in experiments conducted using natural soils [7,43]. This suggests that chemical heterogeneities (i.e., trace element composition, for instance Mn content) of soils may control the mid-term proto-vaterite stabilization.

During burial in soils, granules with proto-vaterite also undergo transformation as well as dissolution processes that increase the granule porosity (Figs. S3B, S4B). In this context, transformation of vaterite into calcite occurs via dissolution/co-precipitation reactions in a similar way as described for the latest stages of the Mn-free pathway. Precursor phases reorganize and crystallize to form calcite crystals with mesoporous faces (Fig. S5I). Later, ion-by-ion growth partially closes this porosity (by cementation) leading to the formation of flat-faced rhombohedra (Fig. S5J).

It should be underlined that part of the trace elements and organic components incorporated into proto-vaterite are transferred to the newly formed calcite crystals as indicates their luminescence and micro-banding chemical composition (Fig. S3). The mechanism through which such transfer take place is not totally understood, although it most likely involves a tight coupling between the dissolution of vaterite and the crystallization of calcite. Indeed, there numerous examples of interface-coupled dissolution–precipitation reactions where sub-micron structural chemical features of the parent phase are transferred to the product one [77–81].

The results presented here emphasize that earthworm-produced biogenic ACC and the transformation processes undergone by $CaCO_3$ phases in earthworm-produced granules are highly influenced by physico-chemical features of the soil where earthworms develop their vital activities setting up a natural laboratory for studying phase transformations and metastability phenomena in biogenic calcium carbonates.

## Declaration of Competing Interest

The authors declare that they have no known competing financial interests or personal relationships that could have appeared to influence the work reported in this paper.

## Acknowledgments

This work was supported by the National Science Center (Poland) grant 2017/25/B/ST10/02221 and by the Ministry of Science, Innovation and Universities (Spain) projects CGL2016-77138-C2-1-P and PID2021-125467NB-I00. We thank the anonymous reviewers and the editor for their help and constructive comments on the text.

## Supplementary materials

Supplementary material associated with this article can be found, in the online version, at doi:10.1016/j.actbio.2023.03.034.

## References


[1] H. Lowenstam, S. Weiner, On Biomineralization, Oxford University Press, New York, 1989 http://site.ebrary.com/id/10087158.

[2] J. Stolarski, I. Coronado, J.G. Murphy, M.V. Kitahara, K. Janiszewska, M. Mazur, A.M. Gothmann, A.S. Bouvier, J. Marin-Carbonne, M.L. Taylor, A.M. Quattrini, C.S. McFadden, J.A. Higgins, L.F. Robinson, A. Meibom, A modern scleractinian coral with a two-component calcite–aragonite skeleton, Proc. Natl. Acad. Sci. U. S. A. (2021) 118, doi:10.1073/pnas.2013316117.

[3] I. Sethmann, G. Wörheide, Structure and composition of calcareous sponge spicules: a review and comparison to structurally related biominerals, Micron 39 (2008) 209–228, doi:10.1016/j.micron.2007.01.006.

[4] G. Falini, S. Fermani, M. Reggi, B. Njegić Džakula, D. Kralj, Evidence of structural variability among synthetic and biogenic vaterite, Chem. Commun. 50 (2014) 15370–15373, doi:10.1039/C4CC05054A.

[5] H. Ehrlich, M. Wysokowski, T. Jesionowski, The philosophy of extreme biomimetics, Sustain. Mater. Technol. (2022) e00447.

[6] G. Luquet, Y. Dauphin, A. Percot, M. Salomé, A. Ziegler, M.S. Fernández, J.L. Arias, Calcium deposits in the Crayfish, Cherax quadricarinatus: microstructure versus elemental distribution, Microsc. Microanal. 22 (2016) 22–38, doi:10.1017/S1431927615015767.

[7] M.R. Lee, M.E. Hodson, G. Langworthy, Earthworms produce granules of intricately zoned calcite, Geology 36 (2008) 943–946, doi:10.1130/G25106A.1.

[8] R.W. Gauldie, Effects of temperature and vaterite replacement on the chemistry of metal ions in the otoliths of Oncorhynchus tshawytscha, Can. J. Fish. Aquat. Sci. 53 (1996) 2015–2026, doi:10.1139/cjfas-53-9-2015.

[9] M. Señorale-Pose, C. Chalar, Y. Dauphin, P. Massard, P. Pradel, M. Marín, Monohydrocalcite in calcareous corpuscles of Mesocestoides corti, Exp. Parasitol. 118 (2008) 54–58, doi:10.1016/j.exppara.2007.06.011.

[10] F. Marin, N. Le Roy, B. Marie, P. Ramos-Silva, I. Bundeleva, N. Guichard, F. Immel, Metazoan calcium carbonate biomineralizations: macroevolutionary trends – challenges for the coming decade, Bull. La Soc. Geol. Fr. 185 (2014) 217–232, doi:10.2113/gssgfbull.185.4.217.

[11] S. Weiner, Y. Levi-kalisman, S. Raz, L. Addadi, Biologically formed amorphous calcium carbonate, Connect Tissue Res. 44 (Suppl 1) (2003) 214–218, doi:10.1080/03008200390181681.

[12] J.H.E.E. Cartwright, A.G. Checa, J.D. Gale, D. Gebauer, C.I. Sainz-Díaz, Calcium carbonate polyamorphism and its role in biomineralization: how many amorphous calcium carbonates are there? Angew. Chemie Int. Ed. 51 (2012) 11960–11970, doi:10.1002/anie.201203125.

[13] D.E. Jacob, A.L. Soldati, R. Wirth, J. Huth, U. Wehrmeister, W. Hofmeister, Nanostructure, composition and mechanisms of bivalve shell growth, Geochim. Cosmochim. Acta. 72 (2008) 5401–5415, doi:10.1016/j.gca.2008.08.019.

[14] T. Mass, A.J. Giuffre, C.-Y.Y. Sun, C.A. Stifler, M.J. Frazier, M. Neder, N. Tamura, C.V. Stan, M.A. Marcus, P.U.P.A.P.A. Gilbert, M. Tali, G.A.J. S. Chang-Yu, S.C.A., F.M.J., N. Maayan, T. Nobumichi, S..C.V., M.M.A., G.P.U.P.A., T. Mass, A.J. Giuffre, C.-Y.Y. Sun, C.A. Stifler, M.J. Frazier, M. Neder, N. Tamura, C.V. Stan, M.A. Marcus, P.U.P.A.P.A. Gilbert, Amorphous calcium carbonate particles form coral skeletons, Proc. Natl. Acad. Sci. 114 (2017) E7670–E7678, doi:10.1073/pnas.1707890114.

[15] J.J. De Yoreo, P.U.P.A.P.A. Gilbert, N.A.J.M.J.M. Sommerdijk, R.L. Penn, S. Whitelam, D. Joester, H. Zhang, J.D. Rimer, A. Navrotsky, J.F. Banfield, A.F. Wallace, F.M. Michel, F.C. Meldrum, H. Cölfen, P.M. Dove, Crystallization by particle attachment in synthetic, biogenic, and geologic environments, Science 349 (2015) aaa6760, doi:10.1126/science.aaa6760.

[16] S. Mann, Biomineralization: Principles and Concepts in Bioinorganic Materials Chemistry, Oxford University Press, Oxford, 2001.

[17] S. Bentov, S. Weil, L. Glazer, A. Sagi, A. Berman, Stabilization of amorphous calcium carbonate by phosphate rich organic matrix proteins and by single phosphoamino acids, J. Struct. Biol. (2010) 171, doi:10.1016/j.jsb.2010.04.007.

[18] A. Gal, S. Weiner, L. Addadi, The stabilizing effect of silicate on biogenic and synthetic amorphous calcium carbonate, J. Am. Chem. Soc. (2010) 132, doi:10.1021/ja106883c.

[19] Y.U.T. Gong, C.E. Killian, I.C. Olson, N.P. Appathurai, A.L. Amasino, M.C. Martin, L.J. Holt, F.H. Wilt, P.U.P.A. Gilbert, Phase transitions in biogenic amorphous calcium carbonate, Proc. Natl. Acad. Sci. U. S. A. 109 (2012) 6088–6093, doi:10.1073/pnas.1118085109.

[20] Y. Politi, D.R. Batchelor, P. Zaslansky, B.F. Chmelka, J.C. Weaver, I. Sagi, S. Weiner, L. Addadi, Role of magnesium ion in the stabilization of biogenic amorphous calcium carbonate: a structure–function investigation, Chem. Mater. 22 (2010) 161–166, doi:10.1021/cm902674h.

[21] J. Seto, Y. Ma, S.A. Davis, F. Meldrum, A. Gourrier, Y.-Y. Kim, U. Schilde, M. Sztucki, M. Burghammer, S. Maltsev, C. Jäger, H. Cölfen, Structure-property relationships of a biological mesocrystal in the adult sea urchin spine, Proc. Natl. Acad. Sci 109 (2012) 3699–3704, doi:10.1073/pnas.1109243109.

[22] Y. Politi, R.A. Metzler, M. Abrecht, B. Gilbert, F.H. Wilt, I. Sagi, L. Addadi, S. Weiner, P.U.P.A. Gilbert, Transformation mechanism of amorphous calcium carbonate into calcite in the sea urchin larval spicule, Proc. Natl. Acad. Sci 105 (2008) 17362–17366, doi:10.1073/pnas.0806604105.

[23] S. Weiner, L. Addadi, Crystallization pathways in biomineralization, Annu. Rev. Mater. Res. (2011) 41, doi:10.1146/annurev-matsci-062910-095803.

[24] C. Rodriguez-Navarro, K. Kudłacz, Ö. Cizer, E. Ruiz-Agudo, Formation of amorphous calcium carbonate and its transformation into mesostructured calcite, CrystEngComm 17 (2015), doi:10.1039/c4ce01562b.

[25] L. Addadi, S. Raz, S. Weiner, Taking advantage of disorder: amorphous calcium carbonate and its roles in biomineralization, Adv. Mater. 15 (2003) 959–970, doi:10.1002/adma.200300381.

[26] J. Ihli, W.C. Wong, E.H. Noel, Y.Y. Kim, A.N. Kulak, H.K. Christenson, M.J. Duer, F.C. Meldrum, Dehydration and crystallization of amorphous calcium carbonate in solution and in air, Nat. Commun. 5 (2014) 1–10, doi:10.1038/ncomms4169.

[27] Z. Zou, W.J.E.M. Habraken, G. Matveeva, A.C.S. Jensen, L. Bertinetti, M.A. Hood, C.-Y. Sun, P.U.P.A. Gilbert, I. Polishchuk, B. Pokroy, J. Mahamid, Y. Politi, S.S.S. Weiner, P. Werner, S. Bette, R. Dinnebier, U. Kolb, E. Zolotoyabko, P. Fratzl, A hydrated crystalline calcium carbonate phase: Calcium carbonate hemihydrate, Science 363 (2019) 396–400, doi:10.1126/science.aav0210.

[28] D. Gebauer, P.N. Gunawidjaja, J.Y.P. Ko, Z. Bacsik, B. Aziz, L. Liu, Y. Hu, L. Bergström, C.-W. Tai, T.-K. Sham, M. Edén, N. Hedin, Proto-calcite and protovaterite in amorphous calcium carbonates, Angew. Chemie. 122 (2010) 9073–9075, doi:10.1002/ange.201003220.

[29] O. Sibony-Nevo, I. Pinkas, V. Farstey, H. Baron, L. Addadi, S. Weiner, The pteropod creseis acicula forms its shell through a disordered nascent aragonite phase, Cryst. Growth Des. 19 (2019) 2564–2573, doi:10.1021/acs.cgd.8b01400.

[30] Y. Levi-Kalisman, S. Raz, S. Weiner, L. Addadi, I. Sagi, Structural differences between biogenic amorphous calcium carbonate phases using X-ray absorption spectroscopy, Adv. Funct. Mater. (2002) 12, doi:10.1002/1616-3028(20020101)12:1<43::AID-ADFM43>3.0.CO;2-C.

[31] S. Raz, P.C. Hamilton, F.H. Wilt, S. Weiner, L. Addadi, The transient phase of amorphous calcium carbonate in sea urchin larval spicules: The involvement of proteins and magnesium ions in its formation and stabilization, Adv. Funct. Mater. 13 (2003) 480–486, doi:10.1002/adfm.200304285.

[32] B. Hasse, H. Ehrenberg, J.C. Marxen, W. Becker, M. Epple, Calcium carbonate modifications in the mineralized shell of the freshwater snail Biomphalaria glabrata, Chemistry 6 (2000) 3679–3685, doi:10.1002/1521-3765(20001016)6:20<3679::aid-chem3679>3.0.co;2-%23.

[33] R.T. Devol, C.-Y.Y. Sun, M.A. Marcus, S.N. Coppersmith, S.C.B.B. Myneni, P.U.P.A.P.A. Gilbert, Nanoscale transforming mineral phases in fresh nacre, J. Am. Chem. Soc. 137 (2015) 13325–13333, doi:10.1021/jacs.5b07931.

[34] T. Mass, A.J. Giuffre, C.Y. Sun, C.A. Stifler, M.J. Frazier, M. Neder, N. Tamura, C.V. Stan, M.A. Marcus, P.U.P.A. Gilbert, Amorphous calcium carbonate particles form coral skeletons, Proc. Natl. Acad. Sci. U. S. A. 114 (2017) E7670–E7678, doi:10.1073/pnas.1707890114.

[35] K. Benzerara, R. Bolzoni, C. Monteil, O. Beyssac, O. Forni, B. Alonso, M.P. Asta, C. Lefevre, The gammaproteobacterium Achromatium forms intracellular amorphous calcium carbonate and not (crystalline) calcite, Geobiology 19 (2021) 199–213, doi:10.1111/gbi.12424.

[36] A. Gal, K. Kahil, N. Vidavsky, R.T. Devol, P.U.P.A. Gilbert, P. Fratzl, S. Weiner, L. Addadi, Particle accretion mechanism underlies biological crystal growth from an amorphous precursor phase, Adv. Funct. Mater. (2014) 24, doi:10.1002/adfm.201400676.

[37] A. Gal, S. Weiner, L. Addadi, A perspective on underlying crystal growth mechanisms in biomineralization: Solution mediated growth versus nanosphere particle accretion, CrystEngComm 17 (2015) 2606–2615, doi:10.1039/c4ce01474j.

[38] M.J.I. Briones, E. López, J. Méndez, J.B. Rodríguez, L. Gago-Duport, Biological control over the formation and storage of amorphous calcium carbonate by earthworms, Mineral. Mag. 72 (2008) 227–231, doi:10.1180/minmag.2008.072.1.227.

[39] B.Y.J.D. Robertson, B. Sc, The function of the calciferous glands of earthworms, J. Exp. Biol. 13 (1936) 279–297.

[40] A.J. Morgan, A morphological and electron-microprobe study of the inorganic composition of the mineralized secretory products of the calciferous gland and chloragogenous tissue of the earthworm, Lumbricus terrestris L. - the distribution of injected strontium, Cell Tissue Res. 220 (1981) 829–844, doi:10.1007/BF00210465.

[41] L. Gago-Duport, M.J.I. Briones, J.B. Rodríguez, B. Covelo, Amorphous calcium carbonate biomineralization in the earthworm's calciferous gland: Pathways to the formation of crystalline phases, J. Struct. Biol. 162 (2008) 422–435, doi:10.1016/j.jsb.2008.02.007.

[42] M.G. Canti, T.G. Piearce, Morphology and dynamics of calcium carbonate granules produced by different earthworm species, Pedobiologia (2003) 511–521, doi:10.1078/0031-4056-00221.

[43] M.E. Hodson, L.G. Benning, B. Demarchi, K.E.H. Penkman, J.D. Rodriguez-Blanco, P.F. Schofield, E.A.A. Versteegh, Biomineralisation by earthworms - An investigation into the stability and distribution of amorphous calcium carbonate, Geochem. Trans. 16 (2015) 1–16, doi:10.1186/s12932-015-0019-z.

[44] C. Darwin, The formation of vegetable mould through the action of worms: With observations on their habits, 1881. doi:10.1017/CBO9780511703850.

[45] T.G. Piearce, The calcium relations of selected lumbricidae, J. Anim. Ecol. 41 (1) (1972) 167–188 Published by: British Ecological Society Stable URL https://www.jstor.org/sta .

[46] M.J.I. Briones, T.G. Piearce, Comparative Anatomy of the Calciferous Gland of Lumbricid Earthworms, in: 2011. https://doi.org/10.1007/978-3-642-14636-7_4.

[47] A. Kelly, Beiträge zur mineralogischen Kenntnis der Kalkausscheidungen im Tierreich, Jenaische Zeitschrift Für Naturwiss 35 (1901) 429–494.

[48] J.D. Rodriguez-Blanco, K.K. Sand, L.G. Benning, ACC and vaterite as intermediates in the solution-based crystallization of CaCO3, New Perspect. Miner. Nucleation Growth, 2017, doi:10.1007/978-3-319-45669-0_5.
[49] A. Fraser, D.C. Lambkin, M.R. Lee, P.F. Schofield, J.F.W. Mosselmans, M.E. Hodson, Incorporation of lead into calcium carbonate granules secreted by earthworms living in lead contaminated soils, Geochim. Cosmochim. Acta. 75 (2011) 2544–2556, doi:10.1016/j.gca.2011.02.015.
[50] L. Brinza, J.F. Mosselmans, P. Schofield, P. Quinn, M. Hodson, Strontium incorporation into carbonate granules secreted by earthworms, 2011. 10.13140/2.1.3115.1042.
[51] L. Brinza, P.F. Schofield, M.E. Hodson, S. Weller, K. Ignatyev, K. Geraki, P.D. Quinn, J.F.W. Mosselmans, Combining $\mu$xANES and $\mu$xRD mapping to analyse the heterogeneity in calcium carbonate granules excreted by the earthworm Lumbricus terrestris, J. Synchrotron Radiat. 21 (2014) 235–241, doi:10.1107/S160057751303083X.
[52] F. Bachmann, R. Hielscher, H. Schaeben, Grain detection from 2d and 3d EBSD data-Specification of the MTEX algorithm, Ultramicroscopy 111 (2011) 1720–1733, doi:10.1016/j.ultramic.2011.08.002.
[53] R. Fernández, S. Kvist, J. Lenihan, G. Giribet, A. Ziegler, Sine systemate chaos? A versatile tool for earthworm taxonomy: Non-destructive imaging of freshly fixed and museum specimens using micro-computed tomography, PLoS One 9 (2014), doi:10.1371/journal.pone.0096617.
[54] N.O.E. Vischer, P.G. Huls, C.L. Woldringh, Object-image - an interactive image–analysis program using structured point collection, Bin. Microbiol. 6 (1994) 160–166. https://doi.org/urn:nbn:nl:ui:229-4252.
[55] M.D. Abràmofff, P.J. Magalhães, S.J. Ram, Image processing with ImageJ Part II, Biophotonics Int 11 (2005) 36–43.
[56] V. Barbin, Application of cathodoluminescence microscopy to recent and past biological materials: a decade of progress, Mineral. Petrol. 107 (2013) 353–362, doi:10.1007/s00710-013-0266-6.
[57] R.E. Crang, R.C. Holsen, J.B. Hitt, Calcite production in mitochondria of earthworm calciferous glands, Bioscience 18 (1968) 299–301, doi:10.2307/1294220.
[58] A. Putnis, L. Fernandez-Diaz, M. Prieto, Experimentally produced oscillatory zoning in the (Ba, Sr)SO4 solid solution, Nature 358 (1992), doi:10.1038/358743a0.
[59] M. Prieto, A. Fernández-González, A. Putnis, L. Fernández-Díaz, Nucleation, growth, and zoning phenomena in crystallizing (Ba,Sr)CO3, Ba (SO4,CrO4), (Ba,Sr)SO4, and (Cd,Ca)CO3 solid solutions from aqueous solutions, Geochim. Cosmochim. Acta. (1997) 61, doi:10.1016/S0016-7037(97)00160-9.
[60] M. Prieto, J.M. Astilleros, L. Fernández-Díaz, Environmental remediation by crystallization of solid solutions, Elements (2013) 9, doi:10.2113/gselements.9.3.195.
[61] M.A. Gonçalves, M. Prieto, Development of compositional patterns during the growth of solid solutions from aqueous solutions: a cellular automaton simulation, Cryst. Growth Des. 14 (2014), doi:10.1021/cg500010p.
[62] M. Greiner, X. Yin, L. Fernández-Díaz, E. Griesshaber, F. Weitzel, A. Ziegler, S. Veintemillas-Verdaguer, W.W. Schmahl, Combined influence of reagent concentrations and agar hydrogel strength on the formation of biomimetic hydrogel–calcite composites, Cryst. Growth Des. 18 (2018) 1401–1414, doi:10.1021/acs.cgd.7b01324.
[63] G. Nehrke, P. Van Cappellen, Framboidal vaterite aggregates and their transformation into calcite: a morphological study, J. Cryst. Growth (2006), doi:10.1016/j.jcrysgro.2005.11.080.
[64] J.D. Rodriguez-Blanco, S. Shaw, L.G. Benning, The kinetics and mechanisms of amorphous calcium carbonate (ACC) crystallization to calcite, via vaterite, Nanoscale 3 (2011) 265–271, doi:10.1039/c0nr00589d.
[65] A.V Radha, T.Z. Forbes, C.E. Killian, P.U.P.A. Gilbert, A. Navrotsky, Transformation and crystallization energetics of synthetic and biogenic amorphous calcium carbonate, Proc. Natl. Acad. Sci 107 (2010) 16438–16443, doi:10.1073/pnas.1009959107.
[66] P. Rez, S. Sinha, A. Gal, Nanocrystallite model for amorphous calcium carbonate, J. Appl. Crystallogr. (2014) 47, doi:10.1107/S1600576714018202.
[67] P. Bots, L.G. Benning, J.D. Rodriguez-Blanco, T. Roncal-Herrero, S. Shaw, Mechanistic insights into the crystallization of amorphous calcium carbonate (ACC), Cryst. Growth Des. 12 (2012) 3806–3814, doi:10.1021/cg300676b.
[68] C.Y. Sun, C.A. Stifler, R.V. Chopdekar, C.A. Schmidt, G. Parida, V. Schoeppler, B.I. Fordyce, J.H. Brau, T. Mass, S. Tambutté, P.U.P.A. Gilbert, From particle attachment to space-filling coral skeletons, Proc. Natl. Acad. Sci. U. S. A. (2020) 117, doi:10.1073/pnas.2012025117.
[69] T. Ogino, T. Suzuki, K. Sawada, The formation and transformation mechanism of calcium carbonate in water, Geochim. Cosmochim. Acta. (1987) 51, doi:10.1016/0016-7037(87)90155-4.
[70] L.N. Plummer, E. Busenberg, The solubilities of calcite, aragonite and vaterite in CO2-H2O solutions between 0 and 90°C, and an evaluation of the aqueous model for the system CaCO3-CO2-H2O, Geochim. Cosmochim. Acta. 46 (1982), doi:10.1016/0016-7037(82)90056-4.
[71] G.-T. Zhou, Q.-Z. Yao, S.-Q. Fu, Y.-B. Guan, Controlled crystallization of unstable vaterite with distinct morphologies and their polymorphic transition to stable calcite, Eur. J. Mineral. 22 (2010) 259–269, doi:10.1127/0935-1221/2009/0022-2008.
[72] K.K. Sand, J.D. Rodriguez-Blanco, E. Makovicky, L.G. Benning, S.L.S. Stipp, Crystallization of CaCO 3 in water-Alcohol mixtures: Spherulitic growth, polymorph stabilization, and morphology change, Cryst. Growth Des. 12 (2012) 842–853, doi:10.1021/cg2012342.
[73] H.F. Greer, M.-H. Liu, C.-Y. Mou, W. Zhou, Dipole field driven morphology evolution in biomimetic vaterite, CrystEngComm 18 (2016) 1585–1599, doi:10.1039/C5CE02142A.
[74] D. Konopacka-Łyskawa, Synthesis methods and favorable conditions for spherical vaterite precipitation: a review, Crystals 9 (2019) 223, doi:10.3390/cryst9040223.
[75] N. Nassrallah-Aboukais, A. Boughriet, J. Laureyns, A. Aboukais, J.C. Fischer, H.R. Langelin, M. Wartel, Transformation of vaterite into cubic calcite in the presence of copper (II) species, Chem. Mater. 10 (1998) 238–243.
[76] A.L. Soldati, D.E. Jacob, U. Wehrmeister, W. Hofmeister, Structural characterization and chemical composition of aragonite and vaterite in freshwater cultured pearls, Mineral. Mag. 72 (2008) 579–592, doi:10.1180/minmag.2008.072.2.579.
[77] A. Putnis, C.V. Putnis, The mechanism of reequilibration of solids in the presence of a fluid phase, J. Solid State Chem. 180 (2007), doi:10.1016/j.jssc.2007.03.023.
[78] F. Xia, J. Brugger, Y. Ngothai, B. O'Neill, G. Chen, A. Pring, Three-dimensional ordered arrays of zeolite nanocrystals with uniform size and orientation by a pseudomorphic coupled dissolution -reprecipitation replacement route, Cryst. Growth Des. 9 (2009), doi:10.1021/cg900691a.
[79] E. Ruiz-Agudo, C.V. Putnis, A. Putnis, Coupled dissolution and precipitation at mineral-fluid interfaces, Chem. Geol. (2014) 383, doi:10.1016/j.chemgeo.2014.06.007.
[80] Z. Liu, Z. Zhang, Z. Wang, B. Jin, D. Li, J. Tao, R. Tang, J.J. de Yoreo, Shape-preserving amorphous-to-crystalline transformation of CaCO3 revealed by in situ TEM, Proc. Natl. Acad. Sci. U. S. A. 117 (2020) 3397–3404, doi:10.1073/pnas.1914813117.
[81] C. Tsao, P.-T. Yu, S.-L. Li, I.-J. Hsu, Y.-C. Chuang, C.-K. Chang, S.-J. Chen, J.C.C. Chan, Ambient formation of spherulites of Mg-calcite in an aqueous lipid solution through the interplay between multiple pathways, J. Phys. Chem. C. 124 (2020) 20538–20546, doi:10.1021/acs.jpcc.0c05248.